Simulating Brownian motion in thermally fluctuating viscoelastic fluids by using the smoothed profile method

Nakayama, Yasuya
Department of Chemical Engineering, Kyushu University

Matsuoka, Yuki
Department of Chemical Engineering, Kyushu University

Kajiwara, Toshihisa
Department of Chemical Engineering, Kyushu University

出版情報：Journal of Computational Physics. 509, pp.113035-, 2024-07-14. Elsevier
バージョン：

Journal of Computational Physics 509 (2024) 113035

Contents lists available at ScienceDirect

Journal of Computational Physics

journal homepage: www.elsevier.com/locate/jcp

Simulating Brownian motion in thermally fluctuating viscoelastic fluids by using the smoothed profile method

Yasuya Nakayama [a,*], Yuki Matsuoka [b,a], Toshihisa Kajiwara [a]

[a] Department of Chemical Engineering, Kyushu University, Nishi-ku, Fukuoka, 819-0395, Japan
[b] Corporate Engineering Center, Sumitomo Bakelite Co., Ltd., Shizuoka, 426-0041, Japan

ARTICLE INFO

Keywords:
Thermal fluctuation
Viscoelastic fluids
Suspension
Smoothed profile method
Microrheology

ABSTRACT

To investigate the Brownian motion of individual particles suspended in viscoelastic fluids, the stochastic smoothed profile method (SPm) for direct numerical simulation is developed by extending deterministic SPm for suspensions in viscoelastic media. To simulate viscoelastic flow driven by thermal fluctuations in the suspending medium, the random stress in the fluid momentum equation as well as the random driving force for the conformation tensor in the Oldroyd-B model are incorporated according to the fluctuating hydrodynamics and fluctuating viscoelasticity formalisms. The thermal equilibrium and dynamical properties calculated by using numerical simulations successfully reproduce the analytic predictions, validating the direct simulation for the coupled fluctuating Navier–Stokes and Oldroyd-B equations and for the coupling between the stochastic viscoelastic medium and individual particles. As an application of the stochastic SPm, we investigate finite system-size effects under periodic boundary conditions (PBCs) on the passive microrheological relationship between the mean-square displacement (MSD) of a Brownian particle and the medium's dynamic modulus. Comparing the modulus that was microrheologically calculated from the MSD with the input modulus reveals that the effect of periodic image cell interaction appears not only in the long-time diffusive regime but also in the short-time region. A frequency-dependent finite system-size correction is implemented by phenomenologically extending the long-time diffusive regime correction, allowing passive microrheology analysis under PBCs. This result can be directly applied to other mesoscale numerical simulations including coarse-grained molecular dynamics and dissipative particle dynamics simulations.

1. Introduction

In particle suspensions, the dynamics of small particles mediated by a matrix fluid are essential for understanding and controlling many physicochemical, biological, and industrial applications. For small particles such as nanoparticles and micronparticles, the thermal fluctuation of the matrix fluid becomes relevant, as it induces the Brownian motion of the suspended particles. The Brownian motion of particles is closely related to a wide range of phenomena, such as the aggregation, structure formation, and rheology of suspension systems [1,2]. One particular application of Brownian motion is microrheology [3–9]. Since particle motion due to the thermal fluctuation of the surrounding fluid is affected by the rheological properties of the fluid, the mean-square displacement (MSD)

* Corresponding author.
E-mail addresses: nakayama@chem-eng.kyushu-u.ac.jp (Y. Nakayama), ymatsuoka@sumibe.co.jp (Y. Matsuoka).

https://doi.org/10.1016/j.jcp.2024.113035
Received 24 March 2023; Received in revised form 3 April 2024; Accepted 17 April 2024

Available online 22 April 2024

of a suspended particle can be related to the frequency-dependent rheological response of the fluid. Microrheology is an efficient technique that can be used to evaluate the rheology of complex fluids. Originally, the MSD was regarded as a similar quantity to the creep compliance of the matrix fluid in the generalized Stokes–Einstein relation (GSER) [3,4], which is only applicable to a limited low-frequency domain. Later, an improved method applicable to high-frequency responses was derived based on the analysis of the generalized Langevin equation (GLE) [10,11], which includes the particle and fluid inertia and hydrodynamic interactions. The basic assumption of microrheology is the application of the GSER or GLE to fluids with a complex rheology. To obtain a fundamental understanding of the effects of the fluid's thermal fluctuation on Brownian motion and its related phenomena, the particle dynamics in thermally fluctuating fluids should be analyzed.

Although the thermal fluctuation in the matrix is a fast process at molecular scales, the Brownian motion of the particles involves different, much slower timescales due to hydrodynamic interactions and inertial effects. In a Newtonian matrix, hydrodynamic interactions cause a power-law correlation in the particle velocity called a long-time tail [12,13]. In complex fluids, such as polymer solutions and melts, another timescale, the structural relaxation time of the fluid, comes into play, and thus the viscoelastic rheology affects the hydrodynamic fluctuation. To analyze Brownian motion in a viscoelastic fluid, the appropriate computational modeling of thermally driven, fluctuating viscoelastic fluids and the coupled dynamics between the fluid and the suspended particle is required.

For a purely viscous Newtonian fluid, several direct numerical simulations (DNSs) of the suspension have been proposed based on the fluctuating Navier–Stokes equation, which satisfies the fluctuation-dissipation relation within the fluid; there are lattice Boltzmann simulations [14,15], a stochastic immersed-boundary method [16–18], and an inertial coupling method [19,20]. For overdamped limit, Brownian Dynamics coupled with fluctuating force-coupling method was explored [21]. Another approach uses the Langevin equation of particles coupled to the Navier–Stokes equation to take into account the hydrodynamic interactions in Brownian motion [22–28].

To consider the viscoelastic effect, the Newtonian fluid model has been extended in different ways. Colored noise with a single relaxation time was applied to a parallel Newtonian–Maxwell fluid without the affine deformation of the displacement field to discuss the spatio-temporal correlation function of hydrodynamic fluctuations [29,30]. In [31], the effect of the fluid's viscoelasticity on the particle motion was considered by introducing a memory kernel and corresponding colored noise. A Markovian fluctuating viscoelastic constitutive model was first derived in the works by Vázquez-Quesada et al. [32]. They derived the fluctuating evolution of the eigenvectors of the conformation tensor that follows the Oldroyd-B model based on GENERIC formalism [33]. Their stochastic differential equation was implemented in the smoothed particle hydrodynamics (SPH) model, which is an Lagrangian flow solver [32], and then was applied to the analysis of Brownian motion of a single particle to test the GSER [34]. Meanwhile, regarding the Eulerian description, fluctuating models expressed as stochastic partial differential equations were derived for viscoelastic constitutive models based on the conformation tensor, such as the Oldroyd-B model, the FENE-P model, and the Giesekus model [35–38]. After the development of the Lagrangian fluctuating viscoelastic simulation with SPH, there is no suspension DNS of viscoelastic fluids based on the Eulerian description using stochastic partial differential equations.

In this article, a DNS to simulate suspension in a thermally fluctuating viscoelastic fluid is developed based on the smoothed profile method (SPm) [39–42]. The matrix fluid is described by the fluctuating Navier–Stokes equation and fluctuating rheological constitutive equation, where the flow and the conformation tensor are driven by thermal fluctuations that satisfy fluctuation-dissipation relations. The dynamics of suspended particles are coupled to the matrix fluid by the SPm; the fluctuating stress drives the random motion of the particles, and simultaneously, the viscoelastic hydrodynamic interaction effects are resolved. To verify the numerical solutions of the fluctuating fluid equations without particles, the spatio-temporal correlation functions of the hydrodynamic fluctuations are calculated and compared with the theoretical solutions. Then, using the developed stochastic SPm, the Brownian motion of a single particle immersed in Newtonian and Oldroyd-B fluids is numerically simulated, and its translational and rotational statistics are compared with the solutions of the GLE.

Finally, a passive microrheology analysis based on the GLE rather than the GSER is applied to simulated Brownian motion in Oldroyd-B fluids. The GLE describes the dynamics of a particle immersed in an infinite sea of suspending fluid. From a computational point of view, to discuss the bulk rheological characteristics, periodic boundary conditions (PBCs) rather than an unbounded boundary are used in most cases. In the past, the application of the GSER to Brownian motion under PBCs in a fluid simulation with smoothed particle hydrodynamics [34] and in molecular dynamics simulations [43,44] resulted in an overestimation of the dynamic modulus in the low-frequency terminal region. To study the finite system-size effects under PBCs on the microrheology at higher frequencies than those in the terminal region, GLE-based microrheology should be considered. The applicability of GLE-based microrheology to Brownian motion under PBCs has not yet been elucidated. The dynamic modulus from the GLE-based microrheology is compared with the input modulus to clarify the finite system-size effects on the microrheology under PBCs. A phenomenological frequency-dependent correction is proposed to extract the dynamic modulus from Brownian motion under PBCs.

2. Fluctuating Navier–Stokes equation and viscoelasticity

The solid particle domain is represented by a density function $\phi(\boldsymbol{r},t) \in [0,1]$, which is equal to one inside of the particle and zero outside of the particle. For ϕ in the SP method, instead of a sharp interface, a diffuse interface domain with a scale ξ is explicitly introduced. The details of the specific definition of ϕ are reported in [39]. The velocity field is defined over the whole domain to include both the matrix fluid and the particles as follows:

$$\boldsymbol{u}(\boldsymbol{r},t) = (1-\phi)\,\boldsymbol{u}_f + \phi \boldsymbol{u}_p, \tag{1}$$

where $\boldsymbol{u}_f$ represents the velocity in the matrix fluid domain; the particle velocity field $\phi\boldsymbol{u}_p$ is constructed with the positions and velocities of the particles, and it is explained later in Section 3. In this section, the governing equations for the continuum variables $\boldsymbol{u}$ and the conformation tensor $\boldsymbol{C}$ which describes the elasticity due to the polymer are explained.

The velocity field is governed by the Navier–Stokes equation, with thermally fluctuating stress in the form of a stochastic differential equation, and the mass continuity equation:

$$\rho_f \mathrm{d}\boldsymbol{u} = \left[-\rho_f \boldsymbol{u}\cdot\nabla\boldsymbol{u} - \nabla p + \nabla\cdot\left(2\eta_s \boldsymbol{D} + \boldsymbol{\sigma}_p\right)\right]\mathrm{d}t + \nabla\cdot\mathrm{d}\boldsymbol{\sigma}^r + \rho_f\phi\boldsymbol{f}_p\mathrm{d}t, \tag{2}$$

$$\nabla\cdot\boldsymbol{u} = 0, \tag{3}$$

where ρ_f, p, η_s, $\boldsymbol{D} = \left(\nabla\boldsymbol{u} + \nabla\boldsymbol{u}^t\right)/2$, and $\boldsymbol{\sigma}_p$ are the fluid mass density, the pressure, the solvent viscosity, the strain-rate tensor, and the viscoelastic stress, respectively; $(.)^t$ indicates a transpose. The body force $\phi\boldsymbol{f}_p$ is a penalty force that is used to enforce the rigid-body constraints within the particle domain; the implementation of this force is explained later in Section 3. The fluctuating stress increment $\mathrm{d}\boldsymbol{\sigma}^r$ is a spatio-temporally white random process whose variance is determined by the fluctuation–dissipation relation as follows [45]:

$$\left\langle \mathrm{d}\sigma^r_{ij}(\boldsymbol{r},t)\right\rangle = 0, \tag{4}$$

$$\left\langle \mathrm{d}\sigma^r_{ij}(\boldsymbol{r},t)\mathrm{d}\sigma^r_{kl}(\boldsymbol{r}',t')\right\rangle = \frac{2\eta_s k_B T(1-\phi)}{V_{\mathrm{cell}}}(\delta_{ik}\delta_{jl}+\delta_{jk}\delta_{il})\delta_{\boldsymbol{r},\boldsymbol{r}'}\delta_{t,t'}\mathrm{d}t, \tag{5}$$

where $\langle\cdot\rangle$ denotes the statistical average, k_BT is the thermal energy, and δ_{ij} is the Kronecker's delta symbol; V_{cell} is the representative volume associated with a single node in discretized space, and $\delta(\boldsymbol{r}-\boldsymbol{r}') \approx \delta_{\boldsymbol{r},\boldsymbol{r}'}/V_{\mathrm{cell}}$. Eq. (5) implies that $\mathrm{d}\boldsymbol{\sigma}^r$ is symmetric. In Eq. (2), $\mathrm{d}\boldsymbol{\sigma}^r$ is additive, *i.e.*, it does not depend on the velocity or pressure.

For the calculation of thermally driven viscoelastic fluids, several methodologies have been proposed to satisfy the fluctuation-dissipation theorem [29,30,32,46,34–37,31,47,48]. In this study, as a constitutive model, the fluctuating Oldroyd-B model [35–38] is considered. In this model, the stress is a function of the conformation tensor, and the conformation tensor evolves according to the thermal fluctuation as follows:

$$\boldsymbol{\sigma}_p = \frac{\eta_p}{\lambda}\left(\boldsymbol{C} - \nu_p\boldsymbol{I}\right), \tag{6}$$

$$\mathrm{d}\boldsymbol{C} = \left(-\boldsymbol{u}\cdot\nabla\boldsymbol{C} + (\nabla\boldsymbol{u})^t\cdot\boldsymbol{C} + \boldsymbol{C}\cdot(\nabla\boldsymbol{u}) - \frac{1}{\lambda}(\boldsymbol{C}-\boldsymbol{I})\right)\mathrm{d}t + \left(\boldsymbol{b}\cdot\mathrm{d}\boldsymbol{W} + \mathrm{d}\boldsymbol{W}^t\cdot\boldsymbol{b}^t\right), \tag{7}$$

$$\left\langle \mathrm{d}W_{ij}(\boldsymbol{r},t)\right\rangle = 0, \tag{8}$$

$$\left\langle \mathrm{d}W_{ij}(\boldsymbol{r},t)\mathrm{d}W_{kl}(\boldsymbol{r}',t')\right\rangle = \frac{k_BT}{\eta_p V_{\mathrm{cell}}}(1-\phi)\,\delta_{ik}\delta_{jl}\delta_{\boldsymbol{r},\boldsymbol{r}'}\delta_{t,t'}\mathrm{d}t, \tag{9}$$

where λ, η_p, and $\boldsymbol{I}$ are the relaxation time, polymer viscosity, and unit tensor, respectively. ν_p in Eq. (6) is a constant factor that determines the free energy minimizer, which is explained in detail in Appendix A. Since we consider a finite number of dumbbells correction [38], $\nu_p < 1$. The systematic part of the right-hand side of Eq. (7) is composed of the advection, affine deformation, and relaxation of $\boldsymbol{C}$. Note that ν_p does not appear explicitly in the relaxation term in Eq. (7). This is because the $(\nu_p - 1)$ term cancels with the Itô drift term resulting from stochastic calculus, which is also explained in detail in Appendix A. The last term in Eq. (7) is the thermal fluctuation derived using the fluctuation–dissipation theorem and the mobility tensor in the relaxation term in the Oldroyd-B model. Here, $\boldsymbol{b}$ is a second-rank tensor that satisfies

$$\boldsymbol{C} = \boldsymbol{b}\cdot\boldsymbol{b}^t. \tag{10}$$

The fluctuation is symmetric and multiplicative, *i.e.*, it explicitly depends on the conformation tensor through $\boldsymbol{b}$ since the mobility tensor in the Oldroyd-B model depends on $\boldsymbol{C}$. The detailed derivation of the fluctuation tensor is explained in Appendix A. In general, according to the Itô calculus for stochastic differential equations, the $\boldsymbol{C}$-dependence of the mobility tensor induces a systematic drift term. In the case of Eq. (7), the Itô drift term cancels the relaxation term by the free energy correction by a finite number of dumbbells [38], so it does not appear explicitly in Eq. (7). As a result, the systematic part of the stochastic differential Eq. (7) is the same as the deterministic Oldroyd-B model (Appendix A).

Here, the ratio of the thermal energy to the elastic energy,

$$\Theta = \frac{k_BT\lambda}{\eta_p V_{\mathrm{cell}}} = \frac{k_BT}{G_p V_{\mathrm{cell}}}, \tag{11}$$

is introduced [35], where $G_p = \eta_p/\lambda$ is the shear modulus. The correction factor in Eq. (6) is $\nu_p = 1 - 4\Theta$, which reflects the fact that the free energy minimizer is $\boldsymbol{C} = \nu_p\boldsymbol{I}$ when the finite-size correction in free energy is considered (Appendix A). As the observation volume becomes smaller, the value of Θ increases, which means the fluctuation becomes more important. This observation suggests that Θ should be sufficiently smaller than 1 for the continuum description of the viscoelasticity to be physically valid. Specifically, by imposing $\nu_p > 0$, an upper bound of $\Theta < 1/4$ can be obtained.

The stochastic differential Eq. (7) requires the calculation of $\boldsymbol{b}$ when the evolution of $\boldsymbol{C}$ is being solved. Instead, the stochastic differential equation in terms of $\boldsymbol{b}$ is derived in [35–38] as follows:

$$\mathrm{d}\boldsymbol{b} = \left(-\boldsymbol{u}\cdot\nabla\boldsymbol{b} + (\nabla\boldsymbol{u})^t\cdot\boldsymbol{b} - \frac{1}{2\lambda}\left(\boldsymbol{b}-\boldsymbol{b}^{-t}\right) - \frac{3\Theta}{2\lambda}\boldsymbol{b}^{-t}\right)\mathrm{d}t + \mathrm{d}\boldsymbol{W}. \tag{12}$$

The systematic part of the right-hand side of Eq. (12) is composed of the advection, deformation, relaxation, and thermal drift of $\boldsymbol{b}$. The thermal fluctuation in Eq. (12) is additive, so the Itô drift does not happen in the $\boldsymbol{b}$ evolution equation. The thermal drift term in Eq. (12) arises from the finite-size correction of the free energy (Appendix A). In this $\boldsymbol{b}$-formulation, $\boldsymbol{C}$ and $\boldsymbol{\sigma}_p$ are obtained using Eqs. (10) and (6). In this formulation, the positive definiteness of $\boldsymbol{C}$ is guaranteed by the definition of Eq. (10), which is advantageous for numerical stability [35,36]. In the deterministic case, the $\boldsymbol{b}$-formulation is as stable as log-conformation formulation [49]. Note that in Eq. (12), unlike the affine deformation of $\boldsymbol{C}$ in Eq. (7), the affine deformation is applied only to the left side of $\boldsymbol{b}$. This is because Eq. (12) is sufficient to derive $\mathrm{d}\boldsymbol{C}$ of Eq. (7) from $\mathrm{d}\boldsymbol{b}$ using Eq. (10).

3. Smoothed profile method for suspension

Consider N_p spherical particles with a radius a, mass M, and moment of inertia $I_p = 2Ma^2/5$ suspended in a thermally fluctuating viscoelastic matrix. The motion of an individual particle is described by

$$\dot{\boldsymbol{R}}_i = \boldsymbol{V}_i, \tag{13}$$

$$M\dot{\boldsymbol{V}}_i = \boldsymbol{F}_i^H + \boldsymbol{F}_i^C, \tag{14}$$

$$I_p\dot{\boldsymbol{\Omega}}_i = \boldsymbol{N}_i^H, \tag{15}$$

where $\boldsymbol{R}_i$, $\boldsymbol{V}_i$, and $\boldsymbol{\Omega}_i$ are the position, velocity, and angular velocity of the i-th particle, respectively, $\boldsymbol{F}_i^H$ and $\boldsymbol{N}_i^H$ are the hydrodynamic force and torque of the fluid [41,50], respectively, which are responsible for the hydrodynamic drag and fluctuating stress, and $\boldsymbol{F}_i^C$ is the sum of all possible inter-particle forces other than the hydrodynamic force acting on ith particle, which is relevant in multi-particle systems. The non-slip boundary condition for the velocity field is assigned at particle surfaces.

We now explain how to solve the system of coupled equations (Eqs. (2)–(12) and (13)–(15)) with the SPm. The SPm provides a way to solve the coupling between solids and fluids, and is applicable to any continuum solvers for fluids [51]. Since this study considers the periodic boundary conditions, the Fourier spectral method is applied to the fluid flow. However, it should be noted that the SPm itself is not limited to the spectral method but can also be applied to other fluid discretization schemes such as finite element/volume method, lattice Boltzmann method, and so on when dealing with other complex boundaries than PBCs. Let $(.)^n$ be a variable at the n-th time step $t_n = nh$ with a time increment h, and let $\widetilde{(f)}_{\boldsymbol{k}}$ be the Fourier transform of the field variable f with the wave vector $\boldsymbol{k}$. In the SPm, the time evolution is performed in a fractional step manner. First, Eq. (2) without the $\phi\boldsymbol{f}_p$-term and Eq. (12) in Fourier space are integrated, and the particle positions are advected. In the Fourier space, Eq. (2) without the $\phi\boldsymbol{f}_p$-term is expressed as

$$\mathrm{d}\widetilde{\boldsymbol{u}}_{\boldsymbol{k}} = -\frac{\eta_s}{\rho_f}k^2\widetilde{\boldsymbol{u}}_{\boldsymbol{k}}\mathrm{d}t + \left[-\widetilde{(\boldsymbol{u}\cdot\nabla\boldsymbol{u})}_{\boldsymbol{k}} - \rho_f^{-1}i\boldsymbol{k}\widetilde{(p)}_{\boldsymbol{k}} + \rho_f^{-1}i\boldsymbol{k}\cdot\widetilde{(\boldsymbol{\sigma}_p)}_{\boldsymbol{k}}\right]\mathrm{d}t + \rho_f^{-1}i\boldsymbol{k}\cdot\widetilde{(\mathrm{d}\boldsymbol{\sigma}^r)}_{\boldsymbol{k}}, \tag{16}$$

the temporal integration of which over h interval can be done as

$$\widetilde{\boldsymbol{u}}_{\boldsymbol{k}}^* = \widetilde{\boldsymbol{u}}_{\boldsymbol{k}}^n\exp\left(-\frac{\eta_s}{\rho_f}k^2h\right) + \int_{t_n}^{t_n+h}\exp\left(-\frac{\eta_s}{\rho_f}k^2\left(t_n+h-t\right)\right)\left[-\widetilde{(\boldsymbol{u}\cdot\nabla\boldsymbol{u})}_{\boldsymbol{k}} - \rho_f^{-1}i\boldsymbol{k}\widetilde{(p)}_{\boldsymbol{k}} + \rho_f^{-1}i\boldsymbol{k}\cdot\widetilde{(\boldsymbol{\sigma}_p)}_{\boldsymbol{k}}\right]\mathrm{d}t$$
$$+ \rho_f^{-1}i\boldsymbol{k}\cdot\int_{t_n}^{t_n+h}\exp\left(-\frac{\eta_s}{\rho_f}k^2\left(t_n+h-t\right)\right)\widetilde{\mathrm{d}\boldsymbol{\sigma}^r}(t).$$

By evaluating the bracket in the second term using the Euler–Maruyama method and performing the stochastic integral of the last term, the following temporal discretization is obtained:

$$\widetilde{\boldsymbol{u}}_{\boldsymbol{k}}^* = \widetilde{\boldsymbol{u}}_{\boldsymbol{k}}^n\exp\left(-\frac{\eta_s}{\rho_f}k^2h\right) + \frac{1-\exp\left(-\frac{\eta_s}{\rho_f}k^2h\right)}{\left(\eta_s/\rho_f\right)k^2}\left[-\widetilde{(\boldsymbol{u}^n\cdot\nabla\boldsymbol{u}^n)}_{\boldsymbol{k}} - \rho_f^{-1}i\boldsymbol{k}\widetilde{(p^n)}_{\boldsymbol{k}} + \rho_f^{-1}i\boldsymbol{k}\cdot\widetilde{\left(\boldsymbol{\sigma}_p^n\right)}_{\boldsymbol{k}}\right]$$
$$+ \sqrt{\frac{1-\exp\left(-2\frac{\eta_s}{\rho_f}k^2h\right)}{2\rho_f\eta_sk^2h}}i\boldsymbol{k}\cdot\widetilde{(\Delta\boldsymbol{\sigma}^{r,n})}_{\boldsymbol{k}}, \tag{17}$$

where the variance of the random stress term is calculated as follows:

$$\left\langle\int_0^h e^{-\frac{\eta_s}{\rho_f}k^2(h-s)}\mathrm{d}\widetilde{\boldsymbol{\sigma}}_{\boldsymbol{k}}^r(t_n+s)\int_0^h e^{-\frac{\eta_s}{\rho_f}k^2(h-u)}\mathrm{d}\widetilde{\boldsymbol{\sigma}}_{\boldsymbol{k}}^r(t_n+u)\right\rangle = \int_0^h e^{-2\frac{\eta_s}{\rho_f}k^2(h-s)}\mathrm{d}s\frac{\left\langle\widetilde{\Delta\boldsymbol{\sigma}^{r,n}}_{\boldsymbol{k}}\widetilde{\Delta\boldsymbol{\sigma}^{r,n}}_{\boldsymbol{k}}\right\rangle}{h}$$

$$= \frac{1-\exp\left(-2\frac{\eta_s}{\rho_f}k^2h\right)}{2\frac{\eta_s}{\rho_f}k^2h}\left\langle \widetilde{\Delta\boldsymbol{\sigma}^{r,n}}_{\boldsymbol{k}}\widetilde{\Delta\boldsymbol{\sigma}^{r,n}}_{\boldsymbol{k}}\right\rangle. \tag{18}$$

Eq. (12) in Fourier space is integrated using the Euler–Maruyama method, and the particle positions are integrated using the second-order Adams–Bashforth method:

$$\widetilde{\boldsymbol{b}}_{\boldsymbol{k}}^{n+1} = \widetilde{\boldsymbol{b}}_{\boldsymbol{k}}^{n} + h\left[-\widetilde{(\boldsymbol{u}^n\cdot\nabla\boldsymbol{b}^n)}_{\boldsymbol{k}} + \left[\widetilde{(\nabla\boldsymbol{u}^n)^t\cdot\boldsymbol{b}^n}\right]_{\boldsymbol{k}} - \frac{1}{2\lambda}\left(\widetilde{\boldsymbol{b}^n}_{\boldsymbol{k}} - \widetilde{\boldsymbol{b}^n}_{\boldsymbol{k}}^{-t}\right) - \frac{3\Theta}{2\lambda}\widetilde{\boldsymbol{b}^n}_{\boldsymbol{k}}^{-t}\right] + \widetilde{\Delta\boldsymbol{W}^n}_{\boldsymbol{k}}, \tag{19}$$

$$\boldsymbol{R}_i^{n+1} = \boldsymbol{R}_i^n + \frac{h}{2}\left[3\boldsymbol{V}_i^n - \boldsymbol{V}_i^{n-1}\right]. \tag{20}$$

Since the thermal driving fields $\Delta\boldsymbol{\sigma}^r$ and $\Delta\boldsymbol{W}$ over h interval are white-in-space (Eqs. (5) and (9)), the full components of $\widetilde{u}_{\boldsymbol{k}}$ and $\widetilde{b}_{\boldsymbol{k}}$ at $|k_x|, |k_y|, |k_z| \le (2\pi/L)(N/2)$ in Fourier space are considered in Eqs. (17) and (19) to satisfy the fluctuation-dissipation relations, where L is the linear system size and $N = L/\Delta$ is the number of grid points with a lattice spacing Δ. In Eqs. (17) and (19), since the random force fields $\Delta\boldsymbol{\sigma}^r$ and $\Delta\boldsymbol{W}$ are additive, whether their generation in the real space or k space leads no difference. For the evaluation of the advection terms in Eqs. (17) and (19), the Orszag's two-thirds rule is applied to suppress the aliasing error [52]. Next, the hydrodynamic force and torque are evaluated according to the change in momentum in the particle domain in real space as follows:

$$\int_{t_n}^{t_n+h} \mathrm{d}t\boldsymbol{F}_i^H = \int \mathrm{d}\boldsymbol{r}\rho_f\phi_i^{n+1}\left(\boldsymbol{u}^* - \boldsymbol{u}_p^*\right), \tag{21}$$

$$\int_{t_n}^{t_n+h} \mathrm{d}t\boldsymbol{N}_i^H = \int \mathrm{d}\boldsymbol{r}\boldsymbol{r}_i^{n+1}\times\rho_f\phi_i^{n+1}\left(\boldsymbol{u}^* - \boldsymbol{u}_p^*\right), \tag{22}$$

where ϕ_i represents the density function of the i-th particle; the intermediate particle velocity field is

$$\phi^{n+1}\boldsymbol{u}_p^* = \sum_{i=1}^{N}\phi_i^{n+1}\left[\boldsymbol{V}_i^n + \boldsymbol{\Omega}_i^n\times\boldsymbol{r}_i^{n+1}\right], \tag{23}$$

where $\boldsymbol{r}_i = \boldsymbol{r} - \boldsymbol{R}_i$. Then, the velocities of the particles are updated to $\boldsymbol{V}_i^{n+1}$ and $\boldsymbol{\Omega}_i^{n+1}$:

$$\boldsymbol{V}_i^{n+1} = \boldsymbol{V}_i^n + M^{-1}\int_{t_n}^{t_n+h}\mathrm{d}t\boldsymbol{F}_i^H + \frac{h}{2}\left[\boldsymbol{F}_i^{C,n+1} + \boldsymbol{F}_i^{C,n}\right], \tag{24}$$

$$\boldsymbol{\Omega}_i^{n+1} = \boldsymbol{\Omega}_i^n + I_p^{-1}\int_{t_n}^{t_n+h}\mathrm{d}t\boldsymbol{N}_i^H, \tag{25}$$

where the potential force $\boldsymbol{F}_i^{C,n}$ is evaluated with the position at $t = t_n$. With the updated particle position and velocity, the updated particle velocity field $\phi^{n+1}\boldsymbol{u}_p^{n+1}$ is obtained. Finally, the velocity field is updated by imposing the rigid-body constraint of the particle velocity field in real space as follows:

$$\boldsymbol{u}^{n+1} = \boldsymbol{u}^* + \int_{t_n}^{t_n+h}\mathrm{d}t\phi\boldsymbol{f}_p, \tag{26}$$

$$\int_{t_n}^{t_n+h}\mathrm{d}t\phi\boldsymbol{f}_p = \phi^{n+1}\left(\boldsymbol{u}_p^{n+1} - \boldsymbol{u}^*\right) - h\rho_f^{-1}\nabla p_p, \tag{27}$$

where p_p is determined by the incompressibility condition $\nabla\cdot\boldsymbol{u}^{n+1} = 0$. Since the viscous stress is applied on not only the fluid domain but also the interface domain (Eq. (17)), the non-slip boundary condition at the particle interface is satisfied within the limits of the interface scale ξ.

Here we discuss the fluctuation-dissipation relations in discretized equations. Since the Fourier transform of the periodic solution is considered, the properties with respect to the spatial derivatives in the continuum equations are preserved in the discretized Eqs. (17) and (19). Specifically, the duality relation between the gradient and divergence operators, which is required for the discrete fluctuation–dissipation relation [53], holds in Eq. (16) as $\widetilde{(\nabla)}_{\boldsymbol{k}} = -\widetilde{(\nabla\cdot)}_{\boldsymbol{k}}^{\dagger}(.)$ since $\widetilde{(\nabla)}_{\boldsymbol{k}} = i\boldsymbol{k}$ where $(.)^{\dagger}$ indicates a adjoint. For the conformation and $\boldsymbol{b}$ tensors, since the irreversible term does not contain the spatial derivative, the fluctuation–dissipation relation also holds in discretized Eq. (19). For the advection terms, the energy conservation is maintained up to the Fourier mode

of $(2/3)(2\pi/L)(N/2)$ since the Orszag's two-thirds rule is used [52]. Based on these points, it is supposed that the fluctuation–dissipation relations in the discretized Eqs. (17) and (19) are maintained.

4. Simulation conditions

Simulations are performed in a three-dimensional cubic domain $\left[-L/2, L/2\right]^3$ with periodic boundary conditions. The simulation domain is uniformly discretized by a lattice spacing Δ, which is chosen to be a unit length. Therefore, the volume associated with a grid is $V_{\mathrm{cell}} = \Delta^3$. The units of time and energy are $\tau = \Delta^2\rho_f/\eta_s$ and $\eta_s\Delta^3/\tau$, respectively. The zero-shear-rate viscosity of the fluid of Eq. (2) is $\eta_0 = \eta_s + \eta_p$, which comes from the solvent and polymer viscosities. The contribution of the solvent viscosity is measured by the viscosity ratio $\beta = \eta_s/\eta_0$, and the polymer viscosity is expressed as $\eta_p = (1-\beta)\eta_0$. The time increment is chosen to be $h = \rho_f/(\eta_0 K_{\max}^2) = \beta\tau/(3\pi^2)$, which is small enough to simulate the momentum diffusion in Eq. (2). The interface scale of the smoothed profile must be larger than the lattice spacing so that the interface domain is supported by grid points. In this work, we set $\xi = 2\Delta$.

Here, we discuss the limitations of the thermal energy in the hydrodynamic models of fluctuating viscoelasticity of Eqs. (7) and (12) according to [35]. Assuming entropic elasticity, and thus $G_p = (N_d/V_{\mathrm{cell}})k_BT$, where the number of dumbbells in a volume V_{cell} is N_d, the non-dimensional temperature is [35]

$$\Theta = \frac{1}{N_d}. \tag{28}$$

This relation implies that the relative importance of the thermal fluctuation directly depends on the observation volume V_{cell} and that at such a small scale, the finite-N_d (finite-size) effect is relevant [38]. In order for the hydrodynamic description of a viscoelastic fluid to be physically valid, $N_d \gg 1$ is required, leading to $\Theta \ll 1$ or, equivalently, $k_BT \ll G_pV_{\mathrm{cell}}$. As mentioned in Section 2, an upper bound $\Theta < 1/4$ is required to define a physically meaningful elastic stress in Eq. (6). As an example of a value of Θ, for a Boger fluid (polymer solution) with $G_p = 1$ Pa at 25 °C, the spatial dimension of $\Delta = 1$ μm yields $\Theta = 4\times10^{-3}$, which implies that the fluctuating viscoelastic hydrodynamics of Eqs. (2) and (7) can be applied to Brownian motion in such a viscoelastic medium.

Another limitation of the thermal energy arises from the inertial effect due to the thermal velocity, $u_T = \sqrt{(2/3)k_BT/\left(\rho\Delta^3\right)}$. In thermally driven flow, the thermal Reynolds number, $Re_T = u_T\Delta/\eta_0$, is much less than unity.

The parameters used to obtain the results in the following section (Section 5) are $\Delta = 1$, $L = 64$, $a = 5$, $\rho_f = \rho_p = 1$, $\eta_s = 1$, and $k_BT = 10^{-4}$. For the Oldroyd-B model, $\beta = 0.1$ ($\eta_p = 9\eta_s$) and $\beta = 0.5$ ($\eta_p = \eta_s$), with $\lambda = 10$ and 10^3, are considered. These parameters give $Re_T = \beta u_T\Delta/\eta_s \ll 1$ and at most $\Theta = k_BT\lambda\beta/(\eta_s(1-\beta)) \le 0.1$. In this parameter setting, several characteristic time scales in the simulation units are estimated as follows: the momentum diffusion time $\tau_s = \rho_f a^2/\eta_s = 25$, the particle inertia time $\rho_p a^2/\eta_s = \tau_s$ (since $\rho_f = \rho_p$ in this work), and the diffusion time $\tau_D = 6\pi\eta_0 a^3/k_BT = 2.36\times10^8$ for $\beta = 0.1$ and 4.71×10^7 for $\beta = 0.5$. To analyze the diffusive regime for a single Brownian particle, the simulation time window should be at least one order larger than the relaxation time, $t > 10\lambda$. This time scale corresponds to $t/h = 3\times10^6$ steps for $\beta = 0.1$ and 6×10^5 steps for $\beta = 0.5$.

For reference, in order to discuss the realistic time scales corresponding to our DNS for $\lambda = 1000$ where the time separation between the relaxation and the momentum diffusion is $\lambda/\tau_s = 40$, dimensional time scales are estimated by assuming a aqueous solution system as a matrix ($\rho_f \approx 1000$ kg/m^3 and $\eta_s \approx 1$ mPa s). By setting the temperature $T = 25$ °C, we obtain $\Delta = 41.2$ nm, $a = 206$ nm, $\tau_s = 42$ ns, $\lambda = 1.7$ μs, $\tau_D = 400$ ms ($\beta = 0.1$), and $\tau_D = 80$ ms ($\beta = 0.5$). Thus, the observation time for this reference system is more than 17 μs.

Furthermore, we here mention the issue of observation time scale when applying our DNS to experimental systems with huge time-scale separation. To exemplify this issue, as a specific example, we consider a Boger fluid reported in Ref. [54], which is composed of PEO, PEG, and water. The fluid parameters of this Boger fluid are $\rho_f = 1035$ kg/m^3, $\eta_0 = 0.066$ Pa s, $\eta_s = 0.047$ Pa s, and $\lambda = 0.0042$ s [54]. By assuming a particle with a radius $a = 5$ μm, we obtain $\tau_s = 551$ ns and $\tau_D = 3.8\times10^4$ s, from which $\lambda/\tau_s = 7629$ is identified. To reach the diffusive regime for this system, at least 8×10^7 steps of time evolution calculations are supposed to be required, that is much larger computational effort than the calculations in this work. Other polymer solution systems can also have larger λ/τ_s than in this work depending on the constituent polymer size and concentration as well as particle size. Such large time scale separations impose significant limitations on the application of DNS in mimicking experimental systems as discussed by Padding and Louis [55]. In such cases, DNS can be used to qualitatively analyze physically relevant processes by telescoping down the time scale separation while maintaining the hierarchy between the multiple time scales, as pointed out in Ref. [55].

To calculate the Wiener processes in Eqs. (5) and (9), the double-precision SIMD (Single Instruction/Multiple Data)-oriented Fast Mersenne Twister (dSFMT) [56] is used to generate pseudo-random numbers with zero mean and unit variance.

5. Results and discussion

5.1. Thermal equilibrium in homogeneous fluids

First, thermally driven homogeneous fluids without suspended particles are simulated to verify the solvers for the fluctuating Navier–Stokes equation (Eq. (2)) and fluctuating Oldroyd-B equation (Eq. (12)). According to the equipartition law, the fluid kinetic energy of a three-dimensional incompressible flow satisfies the following relation:

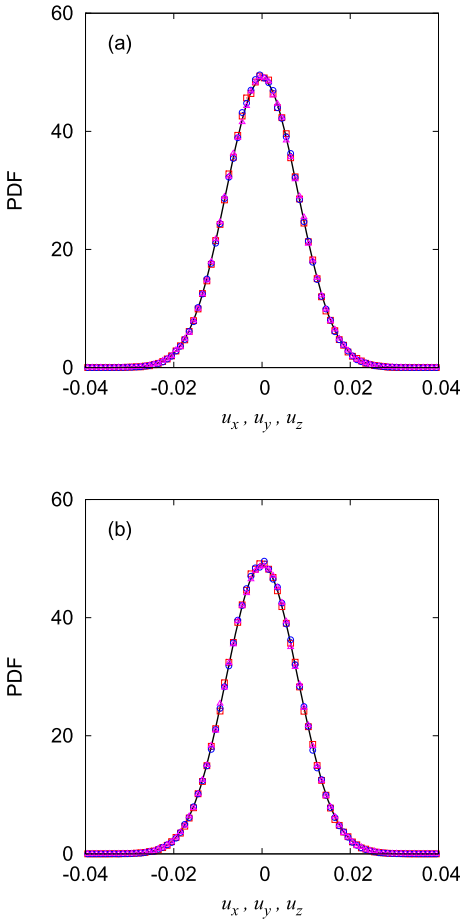

Fig. 1. PDF of each velocity component, u_x (red square), u_y (blue circle), and u_z (pink triangle): (a) fluctuating Newtonian fluid, (b) fluctuating Oldroyd-B fluid with $\lambda = 10$ and $\beta = 0.1$. Theoretical Gaussian PDFs (Eq. (30)) are shown as solid lines. (For interpretation of the colors in the figure(s), the reader is referred to the web version of this article.)

$$\frac{1}{2}\rho_f \langle \boldsymbol{u}^2 \rangle V_{\text{cell}} = k_B T. \tag{29}$$

One degree of freedom of the velocity is constrained by Eq. (3). Fig. 1 shows the probability density functions (PDFs) of three velocity components for the cases of a Newtonian fluid (without $\boldsymbol{\sigma}_p$ and suspended particles in Eq. (2)) and an Oldroyd-B fluid with $\lambda = 10$, $\eta_s = 1$, and $\eta_p = 9\,(\beta = 0.1)$. In Fig. 1, the Gaussian distribution with zero mean and a variance $\langle u_i^2 \rangle = 2k_B T/(3\rho_f V_{\text{cell}})$ derived from Eq. (29),

$$f(u_i) = \sqrt{\frac{3\rho_f V_{\text{cell}}}{4\pi k_B T}} \exp\left(-\frac{3\rho_f V_{\text{cell}} u_i^2}{4k_B T}\right), \tag{30}$$

is also drawn. The PDFs of u_x, u_y, and u_z coincide with the Gaussian distribution, suggesting that the velocity fluctuation is isotropic and that the equipartition law of the fluid kinetic energy (Eq. (29)) is successfully reproduced. Quantitatively, the deviation from Eq. (29) is at most 2%.

The PDFs of C_{xx}, C_{yy}, C_{zz} and C_{xy} are shown in Fig. 2. Eq. (7) predicts that the conformation tensor at the equilibrium state is $\boldsymbol{C}_{\text{eq}} = \boldsymbol{I}$, which suggests that $\langle C_{ii} \rangle = 1$ and $\langle C_{i \neq j} \rangle = 0$. The variances of the components of $\boldsymbol{C}$ at the equilibrium state are $\langle \Delta C_{ii}^2 \rangle = 2\Theta$ and $\langle \Delta C_{i \neq j}^2 \rangle = \Theta$ [37]. The variances of the components of $\boldsymbol{C}$ are also derived from the equipartition law for the conformation tensor in Appendix B. Theoretical PDFs of C_{xx} and C_{xy} can be calculated by marginalizing the equilibrium distribution of $\boldsymbol{C}$, which is a distribution on a six dimensional space and is determined by the free energy density of Eq. (A.8) as follows:

$$p(\boldsymbol{C}) = \frac{1}{Z} \exp\left(-\frac{V_{\text{cell}} \psi(\boldsymbol{C})}{k_B T}\right), \tag{31}$$

where Z is a normalization constant. The PDF of Eq. (31) can be calculated using the Markov chain Monte Carlo (MCMC) method. Technically, MCMC calculation was performed with a decomposed tensor $\boldsymbol{b}$ of Eq. (10) as a random variable and its free energy of Eq. (A.16) to automatically satisfy the positive definiteness of $\boldsymbol{C}$. The theoretical one-dimensional PDFs of C_{xx} and C_{xy} show good

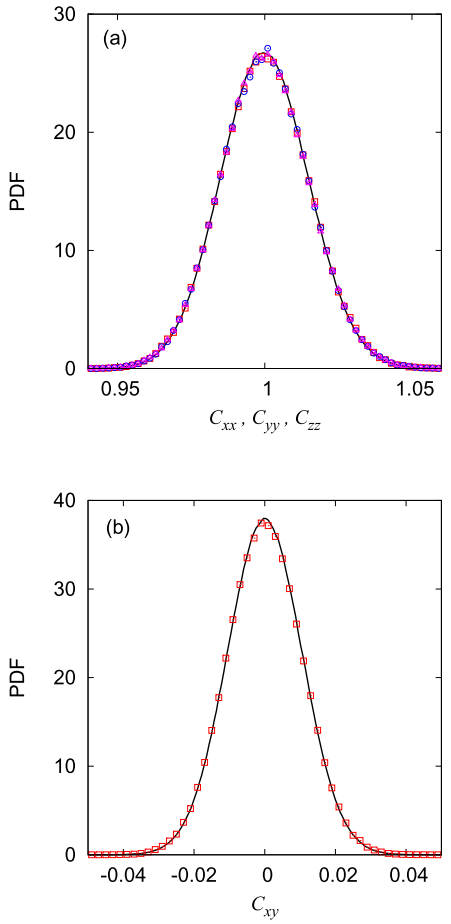

Fig. 2. PDFs of conformation tensor components in the fluctuating Oldroyd-B fluid with $\lambda = 10$ and $\beta = 0.1$:(a) C_{xx} (red square), C_{yy} (blue circle), and C_{zz} (pink triangle), (b) C_{xy} (red square). Equilibrium PDFs (Eq. (31)) calculated using the Monte Carlo method are shown as solid lines.

agreement with those calculated by the DNS, which are shown in Fig. 2. The PDF of a diagonal component in Fig. 2(a) is asymmetric around the mean value of $\langle C_{xx} \rangle = 1$ since the diagonal components of the free energy minimizer $\boldsymbol{C}_{\min}$ (Eq. (A.10)) is smaller than those of $\boldsymbol{C}_{\mathrm{eq}}$ [38]. The asymmetry in C_{xx} PDF becomes more pronounced for an increased Θ as the difference between $\boldsymbol{C}_{\mathrm{eq}}$ and $\boldsymbol{C}_{\min}$ increases. On the other hand, the PDF of a off-diagonal component C_{xy} in Fig. 2(b) is symmetric around its mean $C_{xy} = 0$.

Next, to characterize the thermally driven dynamics of homogeneous fluids governed by Eqs. (2) and (12), the spatio-temporal correlation of the velocity fluctuations is evaluated. Following the definition of the correlation function in molecular liquid theory [57,58] and its hydrodynamic limit, the time correlation function of the Fourier transform of the velocity field is considered:

$$\boldsymbol{u}_{\boldsymbol{k}}(t) = \sum_{\boldsymbol{r}'} \boldsymbol{u}(\boldsymbol{r}', t) \exp\left[-i\boldsymbol{k} \cdot \boldsymbol{r}'\right], \tag{32}$$

$$\frac{k^2}{N} \left\langle u_{\alpha,\boldsymbol{k}}(t) u_{\beta,-\boldsymbol{k}}(0) \right\rangle = \left(\delta_{\alpha\beta} - \frac{k_\alpha k_\beta}{k^2} \right) Z_t(k,t), \tag{33}$$

where $\boldsymbol{k}$ is a wave vector and $k = |\boldsymbol{k}|$; the longitudinal mode vanishes due to the incompressibility condition (Eq. (3)); and $Z_t(k,t)$ denotes the correlation function of transverse modes, which is a scalar function because the fluid dynamics are isotropic.

To discuss the spatio-temporal correlation, a generalized hydrodynamic theory has been proposed in which the shear stress in the hydrodynamic theory is extended to depend on time and space [57,58]:

$$\frac{\partial}{\partial t} Z_t(k,t) = -\nu k^2 Z_t(k,t) - k^2 \int_0^t K(k, t-s) Z_t(k,s) \mathrm{d}s, \tag{34}$$

where $K(k,t)$ is a memory function that depends on time and space. The power spectrum of the dynamics is defined as follows:

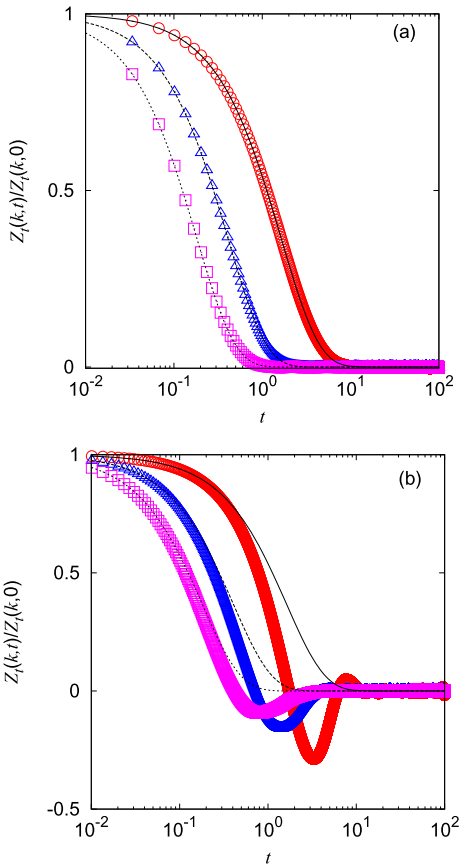

Fig. 3. Time variation of the transverse spatio-temporal correlation function for fluid velocity fluctuations at $k = \pi/4$ (red circle), $\pi/2$ (blue triangle), and $3\pi/4$ (pink square): (a) fluctuating Newtonian fluid, (b) fluctuating Oldroyd-B fluid with $\lambda = 10$ and $\beta = 0.1$. Theoretical predictions from the fluctuating Newtonian fluid (Eq. (39)) are shown as solid ($k = \pi/4$), dashed ($\pi/2$), and dotted ($3\pi/4$) lines.

$$Z_t(k,\omega) = \int_{-\infty}^{\infty} Z_t(k,t)\exp(-i\omega t)\mathrm{d}t. \tag{35}$$

In this framework, the analytical solution of the power spectrum $Z_t(k,\omega)$ of a single-relaxation-mode fluid called the parallel Newtonian-Maxwell model is derived [29,30]; in this model, the Maxwellian elastic stress is added to the Newtonian viscous stress to study the linear hydrodynamics, which correspond to the near-equilibrium dynamics of the fluctuating Oldroyd-B fluid used in this study. The power spectrum for this case is [29,30]

$$Z_t(k,\omega) = Z_t(k,t=0)\frac{2k^2(\nu+\nu^p(\omega))}{\left[\omega - k^2(\omega\lambda)\nu^p(\omega)\right]^2 + \left[k^2(\nu+\nu^p(\omega))\right]^2}, \tag{36}$$

$$\nu^p(\omega) = \mathrm{Re}\left[\frac{\eta^*(\omega)}{\rho_f}\right] = \frac{1}{\rho_f}\frac{\eta_p}{1+\omega^2\lambda^2}, \tag{37}$$

$$\eta^*(\omega) = \frac{\eta_p}{1+i\omega\lambda}, \tag{38}$$

where $\eta^*(\omega)$ is the complex viscosity of the Maxwell model. In the following, to verify the numerical solution of Eqs. (2) and (12), $Z_t(k,t)$ and $Z_t(k,\omega)$ are compared with the theoretical solution of Eq. (34).

Fig. 3(a) shows $Z_t(k,t)/Z_t(k,0)$ for different k; these values were calculated by simulating a fluctuating Newtonian fluid (without $\boldsymbol{\sigma}_p$ and suspended particles in Eq. (2)). The analytical expression of $Z_t(k,t)$ for Newtonian fluids is directly obtained by setting $K = 0$ in Eq. (34) as follows:

$$Z_t(k,t) = Z_t(k,0)\exp(-\nu k^2 t), \tag{39}$$

where $\nu = \eta_s/\rho_f$ is the kinematic viscosity and the k-dependent relaxation time $1/\nu k^2$ is the time required for momentum to diffuse over a spatial scale of $1/k$. The simulation results for different k show single-exponential relaxation and are in good agreement with the theoretical prediction of Eq. (39); the smaller the wavenumber (larger spatial scale), the longer the correlation remains. This

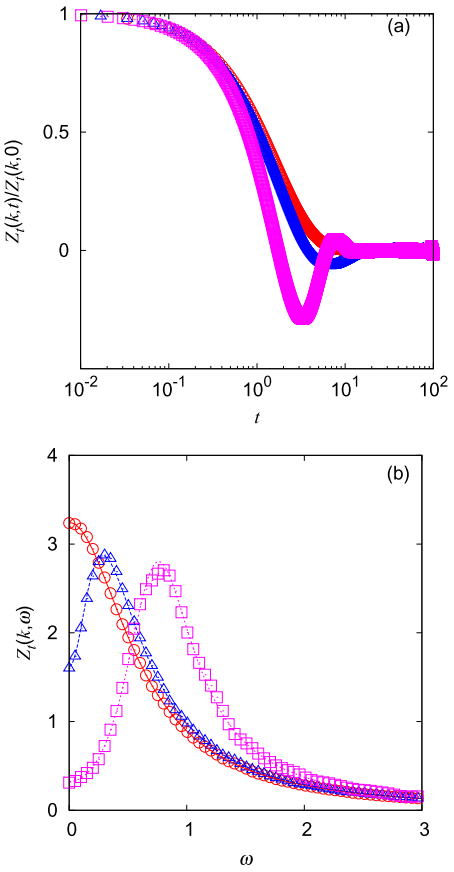

Fig. 4. β-dependence of the transverse spatio-temporal correlation function of fluid velocity fluctuations at the wavenumber $k = \pi/4$: (a) $Z_t(k,t)$, (b) $Z_t(k,\omega)$. Fluctuating Newtonian fluid case with $\eta_s = 1$ is shown as red circle. For fluctuating Oldroyd-B fluids, cases in which $\beta = 0.5$ ($\eta_s = \eta_p = 1$) (blue triangle) and $\beta = 0.1$ ($\eta_s = 1, \eta_p = 9$) (pink square), with $\lambda = 10$, are shown. Theoretical predictions for $Z_t(k,\omega)$ from Eq. (36) are shown as solid (Newtonian), dashed ($\beta = 0.5$), and dotted ($\beta = 0.1$) lines in (b).

quantitative agreement validates the accuracy of the numerical solution of the fluctuating Navier–Stokes equation (Eq. (2)) for a Newtonian fluid system.

Fig. 3(b) shows $Z_t(k,t)/Z_t(k,0)$ for different k for the Oldroyd-B fluid with $\lambda = 10$ and $\beta = 0.1$ that was obtained by solving the fluctuating equations (Eqs. (2) and (12)) without suspended particles. Unlike the simple exponential relaxation observed in the Newtonian fluid, $Z_t(k,t)$ for the Oldroyd-B fluid shows oscillatory behaviors; after an initial exponential decay, a negative correlation appears. For different viscosity ratios β, $Z_t(k,t)$ at $k = \pi/4$ is shown in Fig. 4(a). The polymer viscosity ratio $1-\beta = \eta_p/\eta_0 \in [0,1]$ characterizes the relative contribution of the polymer stress to the viscous stress in the Navier–Stokes equation (Eq. (2)); namely, a large $1-\beta$ indicates a large elasticity contribution to the flow. As $1-\beta$ increases, the oscillatory behavior in $Z_t(k,t)$ becomes more pronounced, and the reversal of $Z_t(k,t)$ becomes large. The power spectrum obtained from the data in Fig. 4(a) is shown in Fig. 4(b). In this Fourier transform, $Z_t(k,t)$ in the long-time domain ($t > 30$), where the correlation can be considered to vanish, is set to zero in order to suppress the high-frequency noise in the calculation of Eq. (35). The power spectra for different β obtained from the simulation results are in good agreement with the theoretical prediction of Eq. (36). The power spectrum for a Newtonian fluid ($\beta = 1$) is of the Lorentzian type, with a peak at $\omega = 0$. On the other hand, $Z_t(k,\omega)$ for an Oldroyd-B fluid ($\beta < 1$) has a peak at finite ω, reflecting the oscillatory decay in $Z_t(k,t)$. As $1-\beta$ increases, the peak frequency increases. The oscillatory relaxation in $Z_t(k,t)$ indicates the memory effect due to the fluid viscoelasticity. The quantitative agreement for the Oldroyd-B fluids validates the accuracy of the numerical solution of the fluctuating Oldroyd-B fluids of Eqs. (2) and (12).

5.2. Brownian motion in a Newtonian fluid

The motion of a single spherical particle immersed in a thermally fluctuating medium is simulated to test the accuracy of the Brownian motion. The volume fraction is $\phi_p = (4/3)\pi(a/L)^3 \approx 0.002$. The velocity autocorrelation function (VACF) and mean-square displacement (MSD) shown below were evaluated by sample averaging of ten independent runs after time averaging of individual particle trajectories.

First, Brownian motion in a Newtonian fluid is considered; the fluctuating Navier–Stokes equation (Eq. (2)) without the viscoelastic stress $\boldsymbol{\sigma}_p$ and the particle equations (Eqs. (13)–(15)) are solved. In a Newtonian solvent system, a relevant timescale is the

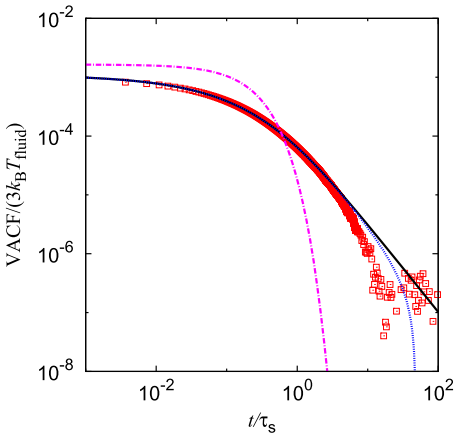

Fig. 5. Translational velocity autocorrelation function (VACF) for a particle suspended in a fluctuating Newtonian medium at a volume fraction of 0.002: DNS results (red open square), the predictions of the Markovian Langevin equation (Eq. (C.10)) (pink dash-dotted line), and the predictions of the generalized Langevin equation (GLE) in the unbounded domain (Eq. (C.12)) (black solid line). The GLE prediction with the finite system-size effect under periodic boundary conditions is also shown as a blue dotted line.

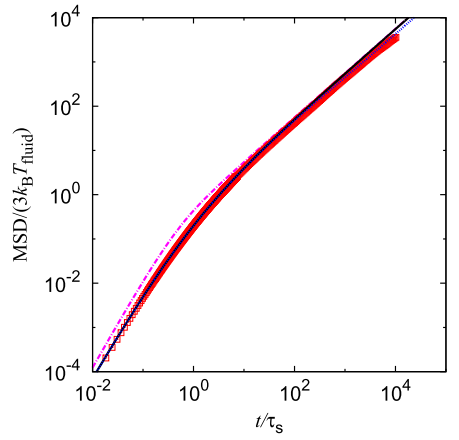

Fig. 6. Translational mean-square displacement (MSD) for a particle suspended in a fluctuating Newtonian medium at a volume fraction of 0.002: DNS results (red open square), the predictions of the Markovian Langevin equation (pink dash-dotted line), and the predictions of the generalized Langevin equation (GLE) in the unbounded domain (black solid line). The GLE prediction with the finite system-size effect under periodic boundary conditions is also shown as a blue dotted line.

momentum diffusion time $\tau_s = \rho_f a^2/\eta_s = 25$. The VACF ($\langle \boldsymbol{V}(t) \cdot \boldsymbol{V}(0) \rangle$) calculated using a numerical simulation and predicted by the standard (LE) and generalized Langevin (GLE) equations with and without finite system-size correction are compared in Fig. 5. The details of the LE and GLE predictions are summarized in Appendix C. The modification of the GLE prediction by the finite system-size effect under PBCs is described in subsection 5.4. In the calculation of the theoretical predictions, the fluid kinetic energy $k_B T_{\text{fluid}} = \rho_f \langle \boldsymbol{u}^2 \rangle V_{\text{cell}}/2$, where the average here is calculated over the fluid region ($\phi = 0$) only, is used to take into account a small numerical error in the simulated temperature ($k_B T_{\text{fluid}} \approx 0.99 k_B T$) (*cf.* subsection 5.1). Since the particle-fluid interface resolution is diffused according to the interface scale ξ in the SP method, the effective particle radius a_{eff} is determined by fitting the MSD at $t \lesssim \tau_s$, which results in a small correction in the particle radius of $a_{\text{eff}} = 1.052a$. The VACF from the numerical simulation is in good agreement with the prediction of the GLE, which includes the effects of the added mass and the Boussinesq–Basset force due to the flow around the particle [59–61]. The VACF from the numerical simulation and the GLE in Fig. 5 also show the power-law behavior of $t^{-3/2}$ at $t \gg \tau_s$, which is called the long-time tail; this behavior is due to the interaction between the momentum diffusion in the fluid caused by the past particle motion and the motion of the current particle [62], which is not explained in the Markovianized LE. The power-law behavior persists in the GLE prediction in the unbounded domain, while it is limited within $\tau_s < t < \rho_f L^2/\eta_0$ both in the DNS result and in the GLE prediction with a finite system-size correction [63].

Fig. 6 shows the MSD of the particle ($\langle \Delta \boldsymbol{R}^2(t) \rangle$, where $\Delta \boldsymbol{R}(t) = \boldsymbol{R}(t_0 + t) - \boldsymbol{R}(t_0)$) calculated by the numerical simulation and the predictions of the LE and GLE with and without a finite system-size correction. The MSD according to the SP method agrees with the prediction of the GLE with a finite system-size correction. In the short-time region $t \ll \tau_s$, the ballistic regime is observed, where $\langle \Delta \boldsymbol{R}^2(t) \rangle = (k_B T_{\text{fluid}}/M_{\text{eff}}) t^2$; its behavior is not affected by the PBCs. In the long-time regime, the diffusive regime is observed; the diffusion constant is extracted using the equation $\langle \Delta \boldsymbol{R}^2(t) \rangle = 6 D^{\text{PBC}} t$, where D^{PBC} is the diffusion constant under the periodic boundary conditions. It is related to the diffusion constant in the infinite domain $D_0 = k_B T_{\text{fluid}}/(6\pi\eta_s a_{\text{eff}})$ via the Stokes–Einstein law as follows [64–68]:

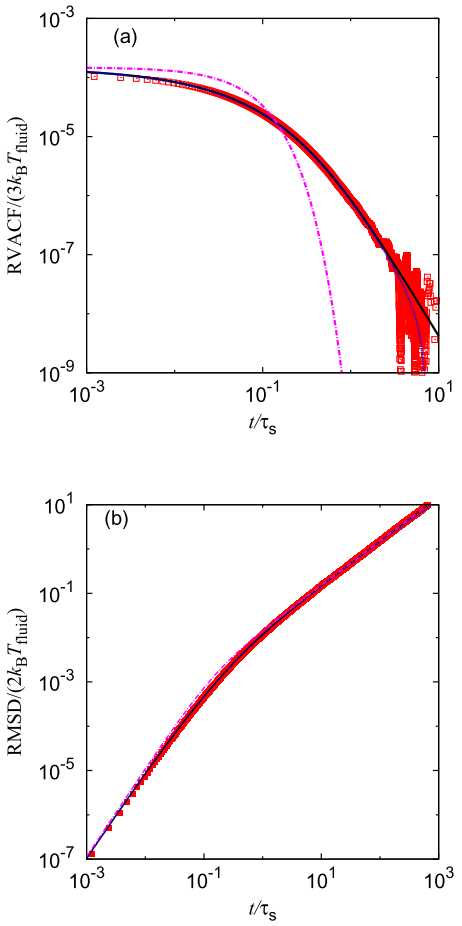

Fig. 7. Rotational Brownian motion of a particle suspended in a Newtonian medium at a volume fraction of 0.002: (a) rotational velocity autocorrelation function (RVACF), (b) rotational mean-square displacement (RMSD). In panels (a) and (b), the DNS results (red open square), the predictions of the Markovian Langevin equation (pink dash-dotted line), the predictions of the generalized Langevin equation (GLE) in the unbounded domain (black solid line), and the GLE prediction with the finite system-size effect under periodic boundary conditions (blue dotted line) are plotted.

$$D^{\mathrm{PBC}} = D_0 \left(1 - \zeta \frac{a_{\mathrm{eff}}}{L}\right), \tag{40}$$

where $\zeta \approx 2.84$. The finite-size correction in Eq. (40) originates from the increased drag caused by the interaction between image cells due to the periodic boundary conditions [64,65,69,67] and results in $D^{\mathrm{PBC}} < D_0$. In our system, the first-order correction is sufficient to describe the DNS result; thus, the higher-order corrections are not considered. The transition from the ballistic regime to the diffusive regime is rather slow compared to the prediction of the LE; this is due to the long-time correlation observed in the VACF as a result of the hydrodynamic interaction. The GLE prediction with the finite system-size correction explains the DNS result well from short to long timescales, while the GLE without correction overestimates the long-term diffusive behavior.

The rotational diffusion of the particle is evaluated similarly to the translational diffusion [70–72]. Fig. 7(a) and (b) shows the autocorrelation function of the angular velocity of the particle (RVACF) $\langle \boldsymbol{\Omega}(t) \cdot \boldsymbol{\Omega}(0) \rangle$ and the rotational mean-square displacement (RMSD) $\langle \Delta \boldsymbol{\phi}^2(t) \rangle$, respectively. A detailed explanation of the rotational diffusion is given in Appendix D. The RMSD and RVACF from the numerical simulation are in good agreement with the prediction of the rotational GLE in the unbounded domain since the finite system-size effect does not apply to rotational diffusive behavior. The agreement of the VACF and MSD for both translational and rotational motion with the theoretical predictions in a Newtonian medium confirms that the proposed SP method reproduces Brownian motion on a wide range of timescales for a particle driven by the thermally fluctuating Navier–Stokes equation (Eq. (2)).

5.3. Brownian motion in a viscoelastic fluid

Next, Brownian motion of a single spherical particle in Oldroyd-B fluids with different viscosity ratios β is considered; the solvent and polymer viscosities are set to $\eta_s = \eta_p = 1$ for $\beta = 0.5$ and $\eta_s = 1$ and $\eta_p = 9$ for $\beta = 0.1$. The relaxation time for both cases is set to $\lambda = 1000$. Fig. 8 shows a sample path of $\Delta \boldsymbol{R}(t)$ projected on the xy-plane during a time interval $\Delta t = 20000 = 20\lambda$ for $\beta = 0.1, 0.5$, and 1 (Newtonian medium). As β decreases, the spatial extension of the trajectory becomes compact. The MSD and VACF calculated by the simulations with $\beta = 0.1$ and 0.5 are compared with the predictions of the GLE (Appendix C) with and without a finite system-size

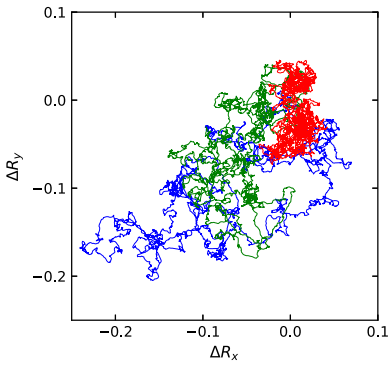

Fig. 8. Time evolution of the particle displacement projected onto the xy-plane. The particle displacements from a certain time origin t_0 up to $t - t_0 = 20\lambda$ are shown for Newtonian medium (blue) and Oldroyd-B media with $\beta = 0.5$ (green) and 0.1 (red).

correction in Fig. 9 for the translational motion and in Fig. 11 for the rotational motion, respectively. The same values of $k_B T_{\text{fluid}}$ and a_{eff} used for the Newtonian medium were also employed in evaluations of the simulation results and theoretical predictions for viscoelastic media. The simulation results for viscoelastic media are in good agreement with the GLE predictions with a finite system-size correction, which validates the numerical solutions of Brownian motion in the fluctuating Oldroyd-B fluid of Eqs. (2) and (12) calculated with the SP method.

In the MSD and RMSD for the Oldroyd-B media ($1 - \beta = \eta_p/\eta_0 > 0$), a subdiffusive region emerges after the ballistic region ($t \gg \tau_s$) at $\beta\lambda < t < \lambda$ due to the viscoelastic relaxation of the fluid [73]. As $1 - \beta$ increases, such plateau regions become apparent. Since the hydrodynamic memory effect persists, the plateau region in the MSD is not flat [73]. When hydrodynamic memory is neglected, a flat plateau region due to viscoelastic relaxation is expected [73–76]. At $t \gg \lambda$, where the elastic deformation in the fluid relaxes, the diffusive behavior follows the plateau region. Due to the slow growth of the MSD in the plateau region, the diffusion constant becomes small for an increased $1 - \beta$ and a fixed η_s.

In the VACF and RVACF for the Oldroyd-B media (Figs. 9(a) and 11(a)), an oscillatory behavior emerges at $t > \tau_s$; this behavior is more pronounced for an increased $1 - \beta$. The power spectra of the particle translational/angular velocity fluctuation are plotted in Fig. 10(a) and (b), respectively. For $1 - \beta > 0$, the peak at finite $\omega \in (1/\lambda, 1/\tau_s)$ emerges in the power spectrum, and it characterizes the anti-correlation in the VACF and RVACF. As $1 - \beta$ increases, the peak frequency increases, indicating the enhanced particle velocity reversal with an increased viscoelastic contribution. The decreased power at low frequencies is simply due to the increase of $\eta_0 = \eta_s/\beta$. The emergence of the anti-correlation in the particle velocity (Fig. 9(b)) and the velocity Fourier mode in homogeneous fluids (Fig. 4 in subsection 5.1) originates from structural relaxation, which causes delayed feedback from the conformation to the flow. This particle velocity reversal in the Oldroyd-B media is responsible for the emergence of the plateau region in the MSD. The transient suppression of the particle motion was experimentally observed for Brownian particles in a wormlike micelle solution of cetyltrimethylammonium bromide (CTAB)-potassium bromide (KBr), a kind of viscoelastic fluid [77]. A similar MSD plateau has also been observed in various systems, such as cell systems [78] and colloidal glass systems [79], although the detailed physics of the suppression of the particle mobility can vary depending on the system.

5.4. Passive microrheology

Microrheology is an experimental technique for the evaluation of the rheological response of complex fluids from the measurement of the motion of a small probe particle [3,4,7–9]. In contrast to the usual rheological measurements in which mechanical deformation is externally applied to the sample, passive microrheology uses the thermal fluctuation of the suspending fluid as the driving force of the probe particle's motion. The response of the particle to the thermal fluctuation is Brownian motion, which is affected by the complex rheology of the suspending fluid and hydrodynamic memory.

The fundamental assumption of passive microrheology is the relation between the MSD or VACF of a probe particle and the complex viscosity $\eta^*(\omega)$ (or equivalently the dynamic modulus $G^*(\omega) = i\omega\eta^*$) of the suspending fluid. One such relation called the "generalized Stokes–Einstein relation (GSER)" was first proposed by Mason and Weitz [3]. The GSER, in terms of the VACF and the dynamic viscosity, can be written as follows:

$$\eta^*_{GSER}(\omega) = \frac{k_B T}{6\pi a \hat{C}_V(\omega)}, \tag{41}$$

where $\hat{C}_V(\omega)$ is the Laplace transform of the VACF (Eq. (C.2)), which can be evaluated with the MSD using the relation $C_V(t) = (1/6)\mathrm{d}^2\langle \Delta\mathbf{R}^2(t)\rangle/\mathrm{d}t^2$ as $\hat{C}_V(\omega) = (i\omega)^2\widehat{\langle \Delta\mathbf{R}^2\rangle}(\omega)/6$. Since the GSER holds only when the fluid and particle inertia are neglected, the applicability of the GSER is limited to the low-frequency response [11,43,34]. Later, based on the VACF equation derived from the GLE (Eq. (C.1)), the GSER was extended to include the particle and fluid inertia by different authors [10,11], allowing it to be applied to a higher frequency range. By applying the frequency-dependent friction (Eq. (C.4)) to the GLE, the full inversion formula can be derived as follows:

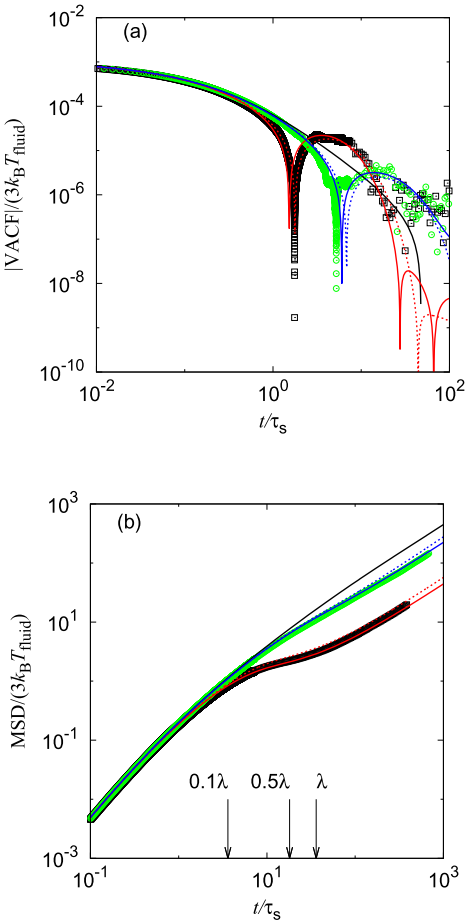

Fig. 9. Translational Brownian motion of a particle suspended in Oldroyd-B media with $\beta = 0.1$ and 0.5 at a volume fraction of 0.002: (a) velocity autocorrelation function (VACF), (b) mean-square displacement (MSD). In panels (a) and (b), the DNS results (black open square ($\beta = 0.1$) and green open circle ($\beta = 0.5$)) and the predictions of the generalized Langevin equation (GLE) in the unbounded domain (red ($\beta = 0.1$) and blue ($\beta = 0.5$) dotted lines) are plotted. The GLE predictions with the finite system-size effect under periodic boundary conditions are also shown as red ($\beta = 0.1$) and blue ($\beta = 0.5$) solid lines. For comparison, the GLE prediction with a finite system-size correction for the Newtonian medium ($\beta = 1$) is also shown as a black solid line.

$$\eta^*(\omega) = f + \frac{i\omega\rho_f a^2}{2} - \sqrt{i\omega\rho_f a^2\left(f + \frac{i\omega\rho_f a^2}{4}\right)}, \tag{42}$$

$$f(\omega) = \eta^*_{GSER}(\omega) - \frac{i\omega M_{\mathrm{eff}}}{6\pi a}. \tag{43}$$

One crucial assumption in the derivation of Eqs. (41) and (42) is the application of the complex viscosity to the GLE for a Newtonian medium. This has been justified using the correspondence principle between Newtonian viscosity and linear viscoelasticity in the small-deformation limit [80,81]. Another assumption is that the GLE describes particle motion in the infinite domain. On the contrary, for the direct simulation of fluctuating fluids, we need to use periodic boundary conditions in most cases. For the long-time diffusion coefficient, the system-size effect caused by image cell interaction reduces the diffusion constant, as indicated by Eq. (40) [64–68]. The finite system-size correction to the GSER (Eq. (41)) was applied to a Brownian particle in a fluctuating smoothed particle hydrodynamics simulation [34] and in a molecular dynamics simulation [44]. The application of the GSER is limited to the low-frequency response and the terminal region of $\omega\lambda \lesssim 1$. To evaluate the high-frequency response at $\omega\lambda > 1$, the full microrheological inversion formula (Eq. (42)) should be applied. However, the effect of PBCs on the complex viscosity of Eq. (42) is not clear. In this subsection, to investigate the effects of PBCs on microrheological inversion, the dynamic viscosity is extracted from the MSD of a simulated Brownian particle in a fluctuating Oldroyd-B fluid.

To apply either the GSER (Eq. (41)) or Eq. (42), the Laplace transform of the MSD should be calculated. In practice, since the measured MSD is subject to statistical errors and the microrheological inversion formula (Eqs. (41)–(42)) uses the second derivative of the MSD, this inversion method is sensitive to the rapid variation in the error in the MSD. To avoid high-frequency statistical errors in the Laplace transform of the MSD, the measured MSD is fitted with the smooth function presented in [43]. The details of the fitting model, including its Laplace transform, are explained in Appendix E.

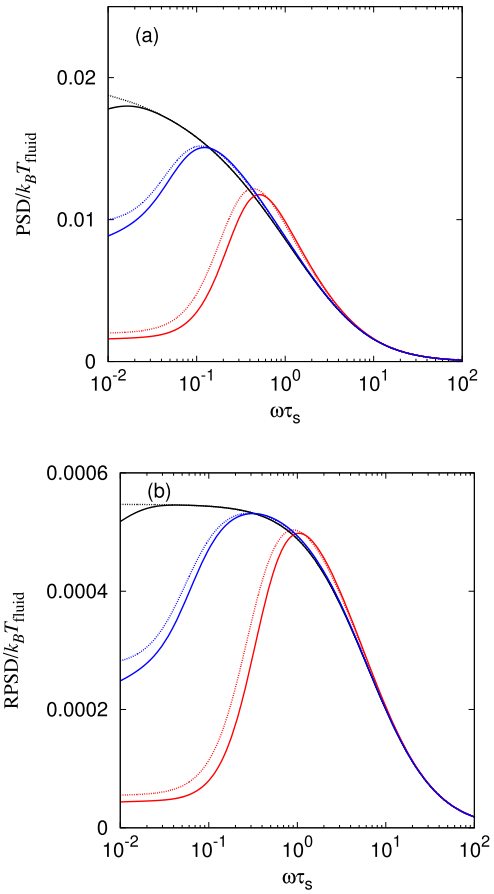

Fig. 10. The power spectral density of (a) the particle velocity fluctuation and (b) the particle angular velocity fluctuation with (solid line) and without (dotted line) a finite system size correction for a Newtonian medium (black) and Oldroyd-B media with $\beta = 0.5$ (blue) and 0.1 (red).

Fig. 12 shows the fitting results for the MSD for Oldroyd-B fluids with $\beta = 0.1$ and 0.5, which are shown in Fig. 9(a). Fig. 13 compares the storage and loss moduli evaluated from the MSD using Eq. (42) with the input dynamic modulus from Eq. (C.15). The relaxation times for inverted moduli are estimated as follows:

$$\lambda_{MR} = \frac{\lim_{\omega\to 0}\eta''_{MR} - \lim_{\omega\to\infty}\eta''_{MR}}{\lim_{\omega\to\infty} G'_{MR}}, \tag{44}$$

where the subscript MR indicates a quantity from the microrheological inversion. The estimated relaxation times are $\lambda_{MR} = 1211$ and 1207 for $\beta = 0.1$ and 0.5, respectively; they are reasonably close to the input relaxation time $\lambda = 1000$. In the terminal region at $\omega\lambda < 1$, using the values of G'_{MR} and G''_{MR} from the microrheological inversion (Eq. (42)) results in overestimation. In contrast, in the high-frequency region at $\omega\lambda > 1$, the loss modulus G''_{MR} shows good agreement with the input G'', while the storage modulus G'_{MR} is still overestimated. These results show that the finite system-size effects on the microrheological inversion of Eq. (42) depend on the frequency.

The overestimation in the terminal region is considered to be due to image cell interaction since the low-frequency response reflects the long-time behavior of the MSD, which was observed in the diffusion constant in Fig. 9(a). Since both the diffusion constant and the loss modulus in the terminal region are related to the zero-shear viscosity ($D = k_BT/(6\pi a\eta_0)$ and $G'' \propto \eta_0\omega$), the finite system-size correction in the terminal region corresponding to Eq. (40) should be $G^*_{\text{MR}}(1 - \zeta a/L) = G^*$. The timescale at which image cell interaction due to momentum diffusion starts to occur is roughly estimated to be $\tau_L = \rho_f L^2/\eta_0$. The finite system-size effects on G^*_{MR} are considered to appear at $\omega \ll 1/\tau_L$. The values of $\lambda_{\text{MR}}/\tau_L$ are 2.9 and 0.6 for $\beta = 0.1$ and 0.5, respectively. A more precise estimation of the threshold timescale for image cell interaction can be performed with the penetration length of the shear wave [82], $\delta(\omega) = \frac{|G^*(\omega)|}{\omega}\sqrt{\frac{2}{\rho}\frac{1}{|G^*(\omega)|+G'(\omega)}}$. The penetration length $\delta(\omega)$ decreases as ω increases, which means that the slower the shear wave from the probe particle, the farther it reaches. The frequency at which the image cell effects appear is estimated from $\delta(\omega) \approx L$, which predicts that the threshold values of $\omega\lambda$ for the finite-size correction are 5.1 and 1.1 for $\beta = 0.1$ and 0.5, respectively. The threshold timescale estimated from the penetration length is consistent with τ_L for the considered cases.

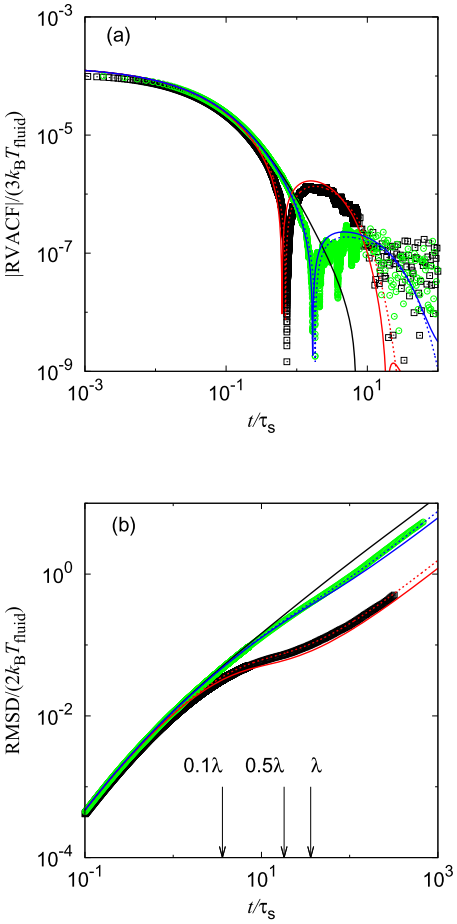

Fig. 11. Rotational Brownian motion of a particle suspended in Oldroyd-B media with $\beta = 0.1$ and 0.5 at a volume fraction of 0.002: (a) rotational velocity autocorrelation function (RVACF), (b) rotational mean-square displacement (RMSD). In panels (a) and (b), the DNS results (black open square ($\beta = 0.1$) and green open circle ($\beta = 0.5$)) and the predictions of the generalized Langevin equation (GLE) in the unbounded domain (red ($\beta = 0.1$) and blue ($\beta = 0.5$) dotted lines) are plotted. The GLE predictions with the finite system-size effect under periodic boundary conditions are also shown as red ($\beta = 0.1$) and blue ($\beta = 0.5$) solid lines. For comparison, the GLE prediction with a finite system-size correction for the Newtonian medium ($\beta = 1$) is also shown as a black solid line.

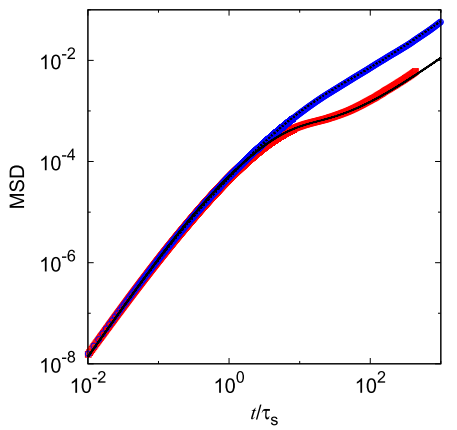

Fig. 12. Fitting Eq. (E.1) to MSD data for Oldroyd-B fluids with $\beta = 0.1$ (solid line) and 0.5 (dotted line), which are presented in Fig. 9(a). The model parameters are $D = 7.19 \times 10^{-8}$, $n = 1$, and $(g_1, \tau_0, \tau_1, \alpha_1) = (2.18 \times 10^{-7}, 3, 100, 1.8)$ for the $\beta = 0.1$ case, and $D = 3.89 \times 10^{-7}$, $n = 2$, and $(g_1, \tau_0, \tau_1, \tau_2, \alpha_1, \alpha_2) = (1.72 \times 10^{-7}, 3, 93.6, 1400, 1.8, 0.638)$ for the $\beta = 0.5$ case.

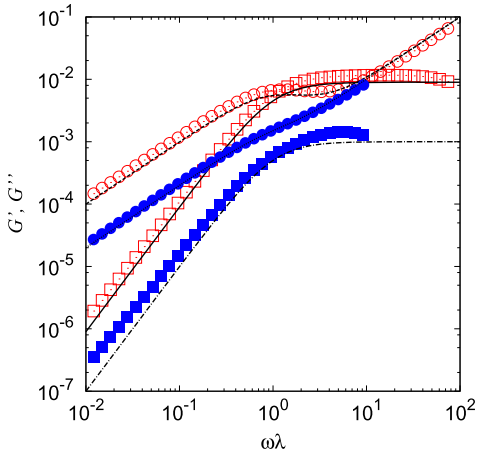

Fig. 13. Comparison of G' and G'' derived from the MSD presented in Fig. 9(a) without a finite system-size correction (red open square (G') and circle (G'') for $\beta = 0.1$ and blue closed square (G') and circle (G'') for $\beta = 0.5$) with the input values of G' and G'' (black lines).

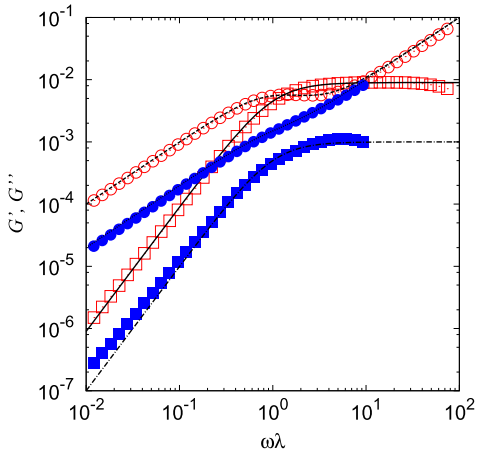

Fig. 14. Comparison of G' and G'' derived from the MSD presented in Fig. 9(a) after the finite system-size correction (Eqs. (46)–(47)) was applied (red open square (G') and circle (G'') for $\beta = 0.1$ and blue closed square (G') and circle (G'') for $\beta = 0.5$) with the input values of G' and G'' (black lines).

At $\omega > 1/\tau_L$, because the momentum diffusion from the probe particle does not reach its image, the loss modulus, which measures the dissipative part of the linear response, is not affected by the PBCs, leading to $G'' \approx G''_{\mathrm{MR}}$. On the other hand, although $\omega > 1/\tau_L$, the overestimation of the storage modulus $G'_{\mathrm{MR}} > G'$ is observed in Fig. 13. Since the elastic stress can affect the image cells due to the pressure wave which is induced by the incompressibility and is transmitted instantaneously. Therefore, the storage modulus at all frequency domain is affected by the finite system size under PBCs.

Based on the observation above, a frequency-dependent finite system-size correction for the loss modulus with a sigmoid function is utilized:

$$h(\omega) = 1 + \exp\left(-\omega\tau_L\right)\left[\left(1 - \zeta\frac{a_{eff}}{L}\right) - 1\right], \tag{45}$$

$$G''(\omega) = G''_{MR}(\omega)h(\omega). \tag{46}$$

For the storage modulus, we perform a uniform correction as follows:

$$G'(\omega) = G'_{MR}(\omega)\left(1 - \zeta\frac{a_{eff}}{L}\right). \tag{47}$$

Since the volume fraction of the probe particle $\phi_p = 0.002$ is in the dilute regime, only a first-order correction $1 - \zeta\frac{a_{eff}}{L}$ is used here. For higher volume fractions, higher-order PBC corrections should be used, as discussed in [44]. Fig. 14 shows the dynamic modulus corrected with Eqs. (46) and (47). The corrected microrheological modulus is in good agreement with the input modulus. This result suggests that the linear rheology can be extracted from Brownian motion under PBCs with a frequency-dependent finite system-size correction.

6. Conclusions

To investigate the Brownian motion of a single spherical particle suspended in viscoelastic fluids, a stochastic smoothed profile method (SPm) for direct numerical simulation was developed by extending the deterministic SPm for suspensions in viscoelastic media [83,84,51]. The Brownian motion of particles is driven by the thermal fluctuation of the suspending viscoelastic medium. To simulate the viscoelastic flow driven by thermal fluctuations, the random stress satisfying the fluctuation–dissipation theorem (FDT), along with the viscous stress is incorporated into the fluid momentum equation based on the formalism known as fluctuating hydrodynamics [85], while the thermal driving force for the conformation tensor that satisfies the FDT with the irreversible conformation relaxation is incorporated into the Oldroyd-B model, a viscoelastic constitutive equation, based on the formalism known as fluctuating viscoelasticity [35,38]. In previous studies on fluctuating viscoelasticity theory, the focus has been mainly on conformation fluctuations under imposed homogeneous flow [36,37], whereas the two-way coupling between the conformation and flow has been only available in SPH model [34] In [32], the stochastic eigenvector dynamics of the conformation tensor in Lagrangian basis was derived based on the GENERIC framework [33], and was implemented in SPH simulation. Subsequently, this fluctuating viscoelastic SPH was firstly applied to simulate the Brownian motion [34]. After this stochastic differential equations in Lagrangian picture, an alternative set of stochastic partial differential equations for fluctuating viscoelasticity in Eulerian picture was derived [35,38]. The stochastic SPm in this work offers an alternative DNS for suspension dynamics based on the Eulerian picture described by stochastic partial differential equations by the fluctuating viscoelasticity theory. Although both SPH simulation in [34] and the stochastic SPm of this work have been applied for analysis of a single Brownian particle, DNS for multi-particle Brownian systems are also available since the non-Brownian multi-particle DNS have already been reported for SPH [86,87] and SPm [84], which use the deterministic parts of their respective thermal fluctuation models.

Since this study considered the flow under periodic boundary conditions, the Fourier spectral method was used to solve the field variables. This implementation is not necessarily suitable when walls are present, although the walls can be handled as a fixed particle objects in the framework of SPm [51]. Other flow solvers such as finite element method and lattice Boltzmann method, than the spectral method can be preferred when dealing with flows in complex geometries. Even in such cases, the SPm can be applied to solve the interaction between particles and flow.

For a homogeneous fluid without particles, from the DNS of the coupled fluctuating Navier–Stokes and Oldroyd-B equations, equilibrium statistics and the spatio-temporal correlation of the flow field were calculated and are in good agreement with the theoretical predictions; these results validate the DNS of thermally driven viscoelastic flow. In suspension in a viscoelastic medium, the Brownian motion of individual suspended particles driven by fluid thermal fluctuations is subject to viscoelastic effects as well as hydrodynamic interactions. The translational and rotational VACF and MSD of a simulated Brownian particle are in good agreement with the solutions of the GLE. These results validate the coupling between thermally driven viscoelastic flow and particle dynamics in our DNS. The calculated Brownian motion successfully reproduced the anti-correlation of particle velocities for translational and rotational VACFs and plateaus for translational and rotational MSDs at time scales below the relaxation time; these are characteristic effects of matrix viscoelasticity. The developed stochastic SPm was confirmed to be able to reproduce the dynamics of Brownian motion in the viscoelastic matrix flow over a wide range of time scales. The fluctuating viscoelasticity theory used in the stochastic SPm has been developed for other viscoelastic models, such as the Giesekus and FENE-P models, in addition to the Oldroyd-B model [38]. Therefore, the stochastic SPm can be extended to these other constitutive equations, enabling the analysis of a wide range of physical phenomena with various viscoelastic models.

As an application of the stochastic SPm, passive microrheology with Brownian motion in a finite-size domain under periodic boundary conditions was investigated. Passive microrheology analysis relates the Brownian motion of a particle and the dynamic modulus of the matrix fluid. Only for the long-term diffusive regime (rheologically low-frequency terminal region) are the effects of periodic boundary conditions well known [64–68,44]. However, the effects of periodic boundary conditions on microrheological analysis in all frequency domains, including the domains at which hydrodynamic interactions and matrix viscoelasticity are dominant, were previously unknown. The microrheological inversion of the MSD under periodic boundary conditions revealed that the image cell effects appeared not only in the diffusive regime but also in the short-time region. In other words, the finite system-size effect in periodic boundary conditions on Brownian motion was found to be frequency-dependent. Based on a comparison of the DNS results under periodic boundary conditions with the analytical solution of the GLE in the infinite domain, a frequency-dependent finite system-size correction was introduced to calculate the dynamic modulus using microrheological inversion from the Brownian motion under periodic boundary conditions. Moreover, by applying the frequency-dependent correction to the GLE, VACF, and MSD of Brownian motion under periodic boundary conditions are predicted. This result can be directly applied to the interpretation of periodic boundary effects in mesoscale numerical calculations, such as those involving coarse-grained molecular dynamics and dissipative particle dynamics, as well as in hydrodynamic simulations, as in this study.

CRediT authorship contribution statement

Yasuya Nakayama: Conceptualization, Data curation, Formal analysis, Funding acquisition, Investigation, Methodology, Project administration, Software, Supervision, Validation, Visualization, Writing – original draft, Writing – review & editing. **Yuki Matsuoka:** Conceptualization, Data curation, Formal analysis, Investigation, Methodology, Software, Validation, Visualization, Writing – original draft, Writing – review & editing. **Toshihisa Kajiwara:** Project administration.

Declaration of competing interest

The authors declare the following financial interests/personal relationships which may be considered as potential competing interests: Yasuya Nakayama reports financial support was provided by Japan Society for the Promotion of Science.

Data availability

Data will be made available on request.

Acknowledgements

The numerical calculations were mainly carried out using the computer facilities at the Research Institute for Information Technology at Kyushu University. This work was supported by Grants-in-Aid for Scientific Research (JSPS KAKENHI) under Grant Nos. JP18K03563 and JP23K03343, and the JSPS Core-to-Core Program "Advanced core-to-core network for the physics of self-organizing active matter (JPJSCCA20230002)".

Appendix A. Fluctuation-dissipation relation in conformation evolution

Let ψ be the free energy density per unit volume. The deterministic evolution of the conformation tensor $\boldsymbol{C}$ is written as follows:

$$\overset{\triangledown}{\boldsymbol{C}} = -\boldsymbol{\Lambda}^{(4)} \odot \frac{\partial \psi}{\partial \boldsymbol{C}}, \tag{A.1}$$

where $\overset{\triangledown}{(.)}$ represents the upper-convected time derivative

$$\overset{\triangledown}{\boldsymbol{C}} \equiv \left(\partial_t + \boldsymbol{u}\cdot\nabla\right)\boldsymbol{C} - \nabla\boldsymbol{u}^t\cdot\boldsymbol{C} - \boldsymbol{C}\cdot\nabla\boldsymbol{u}, \tag{A.2}$$

where the affine deformation of $\boldsymbol{C}$ due to the flow field is assumed; $\boldsymbol{\Lambda}^{(4)}$ is the mobility tensor, which is fourth-rank, and the notation $\left[\boldsymbol{\Lambda}^{(4)} \odot \frac{\partial \psi}{\partial \boldsymbol{C}}\right]_{ij} = \Lambda^{(4)}_{ijkl}\frac{\partial \psi}{\partial C_{kl}}$ is used. Since $\boldsymbol{C}$ is symmetric, $\Lambda^{(4)}_{ijkl}$ must be symmetric about $i \leftrightarrow j$ and $k \leftrightarrow l$. The fluctuating dynamics corresponding to Eq. (A.1) are [88,33]

$$\overset{\triangledown}{\boldsymbol{C}}\,\mathrm{d}t = -\boldsymbol{\Lambda}^{(4)} \odot \frac{\partial \psi}{\partial \boldsymbol{C}}\mathrm{d}t + \frac{k_B T}{V_{\mathrm{cell}}}\frac{\partial}{\partial \boldsymbol{C}} \odot \boldsymbol{\Lambda}^{(4)}\mathrm{d}t + \frac{\boldsymbol{B}^{(4)}}{\sqrt{V_{\mathrm{cell}}}} \odot \mathrm{d}\boldsymbol{w}, \tag{A.3}$$

where the notation $\overset{\triangledown}{\boldsymbol{C}}\,\mathrm{d}t \equiv \mathrm{d}\boldsymbol{C} + \left(\boldsymbol{u}\cdot\nabla\boldsymbol{C} - \nabla\boldsymbol{u}^t\cdot\boldsymbol{C} - \boldsymbol{C}\cdot\nabla\boldsymbol{u}\right)\mathrm{d}t$ is used; $\mathrm{d}\boldsymbol{w}$ represents spatio-temporal Wiener processes with

$$\left\langle \mathrm{d}w_{ij}(\boldsymbol{r},t)\right\rangle = 0, \tag{A.4}$$

$$\left\langle \mathrm{d}w_{ij}(\boldsymbol{r},t)\mathrm{d}w_{kl}(\boldsymbol{r}',t')\right\rangle = \delta_{ik}\delta_{jl}\delta_{\boldsymbol{r},\boldsymbol{r}'}\delta_{t,t'}\mathrm{d}t. \tag{A.5}$$

The amplitude $\boldsymbol{B}^{(4)}$ is a fourth-rank tensor and is specified by the following fluctuation–dissipation relation [88,33]:

$$B^{(4)}_{ijmn}B^{(4)}_{klmn} = 2k_B T\Lambda^{(4)}_{ijkl}. \tag{A.6}$$

The second term on the right-hand side of Eq. (A.3) is the systematic drift derived using Itô calculus, which is relevant when the mobility tensor is explicitly dependent on $\boldsymbol{C}$.

Next, the stochastic differential Eq. (7) in terms of $\boldsymbol{C}$ is derived by applying explicit forms of the free energy and mobility tensor. The mobility tensor of the Oldroyd-B model (which microscopically corresponds to a dumbbell model) is

$$\Lambda^{(4)}_{ijkl} = \frac{1}{2G_p\lambda}\left[\left(C_{ik}\delta_{jl} + C_{jk}\delta_{il}\right) + \left(C_{il}\delta_{jk} + C_{jl}\delta_{ik}\right)\right], \tag{A.7}$$

which is symmetric about $i \leftrightarrow j$ and $k \leftrightarrow l$ [35]. Let us consider a small scale at which thermal fluctuation is relevant. The free energy density for a finite number of dumbbells N_p in a finite volume is [38]

$$\psi(\boldsymbol{C}) = \frac{G_p}{2}\left(\mathrm{tr}\boldsymbol{C} - \ln\det\boldsymbol{C}\right) + \frac{G_p}{2N_p}(d+1)\ln\det\boldsymbol{C} + \mathrm{cst.}, \tag{A.8}$$

where d is the number of spatial dimensions; the first term represents the elastic energy of dumbbells, the second term is from the conformation entropy, and the third term is the finite-N_p (finite-size) correction. The gradient of ψ is

$$\frac{\partial \psi}{\partial \boldsymbol{C}} = \frac{G_p}{2}\left(\boldsymbol{I} - \boldsymbol{C}^{-t}\right) + \frac{G_p}{2N_p}(d+1)\boldsymbol{C}^{-t}, \tag{A.9}$$

from which the minimizer is identified as

$$\boldsymbol{C}_{\min} = (1 - (d+1)\,\Theta)\,\boldsymbol{I}, \tag{A.10}$$

and the polymer stress is

$$\boldsymbol{\tau}_p = 2\boldsymbol{C} \cdot \frac{\partial \psi}{\partial \boldsymbol{C}} \tag{A.11}$$

$$= G\left(\boldsymbol{C} - \nu_p \boldsymbol{I}\right). \tag{A.12}$$

Using Eqs. (A.6), (A.7), and (10), the thermal fluctuation is given by

$$\frac{\boldsymbol{B}^{(4)}}{\sqrt{V_{\text{cell}}}} \odot \mathrm{d}\boldsymbol{w} = \sqrt{\frac{\Theta}{\lambda}}\left(\boldsymbol{b} \cdot \mathrm{d}\boldsymbol{w} + \mathrm{d}\boldsymbol{w}^t \cdot \boldsymbol{b}^t\right). \tag{A.13}$$

The Itô drift term and relaxation terms are

$$\frac{k_B T}{V_{\text{cell}}} \frac{\partial}{\partial C_{ij}} \Lambda^{(4)}_{ijkl} = \frac{\Theta}{\lambda}(d+1)\,\delta_{kl}, \tag{A.14}$$

$$-\Lambda^{(4)}_{ijkl} \frac{\partial \psi}{\partial C_{kl}} = -\frac{1}{\lambda}\left(C_{ij} - \delta_{ij}\right) - \frac{\Theta}{\lambda}(d+1)\,\delta_{ij}. \tag{A.15}$$

We observe that the relaxation term derived from the finite-size correction of the free energy cancels out the Itô drift term. By substituting Eqs. (A.13), (A.14), and (A.15) into Eq. (A.3), the stochastic differential Eq. (7) in terms of $\boldsymbol{C}$ is obtained.

Next, the stochastic differential Eq. (12) in terms of $\boldsymbol{b}$ is derived. To this end, we specify the free energy and mobility tensor in terms of $\boldsymbol{b}$ using a change of variables of Eq. (10) as follows [35]:

$$\tilde{\psi}(\boldsymbol{b}) = \psi(\boldsymbol{C}) - \frac{k_B T}{V} \ln\det \boldsymbol{b} + \text{cst.}, \tag{A.16}$$

$$\tilde{\Lambda}^{(4)}_{ijkl} = \frac{1}{2G_p \lambda}\delta_{ik}\delta_{jl}. \tag{A.17}$$

Here, the $\boldsymbol{b}$-based mobility $\tilde{\Lambda}^{(4)}_{ijkl}$ does not depend on $\boldsymbol{b}$, which implies that the fluctuation is additive and that no Itô drift appears in the $\boldsymbol{b}$ evolution equation. Then, the relaxation of $\boldsymbol{b}$ is obtained as follows:

$$-\tilde{\Lambda}^{(4)}_{ijkl} \frac{\partial \tilde{\psi}}{\partial b_{kl}} = -\frac{1}{2\lambda}\left(b_{ij} - b^{-t}_{ij}\right) - \frac{\Theta d}{2\lambda} b^{-t}_{ij}, \tag{A.18}$$

where a Θ-dependent drift term arises from the finite-size correction of the free energy and an additional entropic term appears due to the change of variables (Eq. (10)). Using the fluctuation–dissipation relation for $\boldsymbol{b}$ dynamics,

$$\tilde{\boldsymbol{B}}^{(4)}_{ijmn}\tilde{\boldsymbol{B}}^{(4)}_{klmn} = 2k_B T \tilde{\Lambda}^{(4)}_{ijkl} \tag{A.19}$$

$$= \frac{k_B T}{G_p \lambda}\delta_{ik}\delta_{jl}, \tag{A.20}$$

the thermal fluctuation is identified as follows:

$$\frac{\boldsymbol{B}^{(4)}}{\sqrt{V_{\text{cell}}}} \odot \mathrm{d}\boldsymbol{w} = \sqrt{\frac{\Theta}{\lambda}}\mathrm{d}\boldsymbol{w}. \tag{A.21}$$

By combining Eqs. (A.18) and (A.21), the stochastic differential Eq. (12) is obtained.

Appendix B. Equipartition law for the conformation tensor

At close to equilibrium, the conformation tensor fluctuates around its mean $\boldsymbol{C} = \boldsymbol{I}$, which is derived by averaging Eq. (7) without flow. In this linear response regime, the free energy is approximated by the following quadratic form:

$$\psi \approx \frac{G_p}{2}(\boldsymbol{C} - \boldsymbol{I}) : (\boldsymbol{C} - \boldsymbol{I}). \tag{B.1}$$

Since $\boldsymbol{C}$ is symmetric, it has six degrees of freedom, so $\langle\psi\rangle V_{\text{cell}} = 6k_B T$ holds by the equipartition law. Due to the symmetry of $\boldsymbol{C}$, the components of $\langle\psi\rangle$ are

$$\frac{G_p}{2}\langle\left(C_{ii} - 1\right)^2\rangle V_{\text{cell}} = k_B T, \tag{B.2}$$

$$\frac{G_p}{2}\langle\left(C_{i\neq j} + C_{ji}\right)^2\rangle V_{\text{cell}} = k_B T, \tag{B.3}$$

from which the variances of the components of $\boldsymbol{C}$ are obtained as follows:

$$\langle \left(C_{ii} - 1\right)^2 \rangle = 2\Theta, \tag{B.4}$$

$$\langle \left(C_{i\neq j}\right)^2 \rangle = \Theta. \tag{B.5}$$

Appendix C. Brownian motion and generalized Langevin equation of a particle

According to the generalized Langevin equation of a particle immersed in an incompressible flow, the velocity autocorrelation function (VACF) in one direction $C_V(t) = \langle V_x(t)V_x(0)\rangle$ is

$$M_{\text{eff}}\frac{\mathrm{d}C_V}{\mathrm{d}t} = -\int_0^t \mathrm{d}s\zeta(t-s)C_V(s), \tag{C.1}$$

where $M_{\text{eff}} = M + (2/3)\pi a^3\rho_f$ and ρ_f, the fluid mass density, includes the added mass effect due to the replaced fluid acceleration; $\zeta(t)$ is a time-dependent friction coefficient. The Laplace transform of Eq. (C.1) leads to

$$\hat{C}_V(\omega) = \left[\int_0^\infty \mathrm{d}tC_V(t)\exp(-zt)\right]_{z=i\omega} \tag{C.2}$$

$$= \frac{k_BT}{i\omega M_{\text{eff}} + \zeta(\omega)}, \tag{C.3}$$

where $C_V(t=0) = \langle V_x^2\rangle = k_BT/M_{\text{eff}}$ is used; the friction coefficient is represented as follows [85]:

$$\zeta(\omega) = 6\pi a\eta^*(\omega)\left(1 + \sqrt{i\omega\rho_f a^2/\eta^*(\omega)}\right), \tag{C.4}$$

where $\eta^*(\omega)$ is the complex viscosity of the fluid. Once $\eta^*(\omega)$ is specified, the VACF $C_V(t)$ is obtained using the inversion formula as follows:

$$C_V(t) = \int_{-\infty}^\infty \frac{\mathrm{d}\omega}{\pi}\mathrm{Re}\left[\hat{C}_V(\omega)\right]\cos\omega t. \tag{C.5}$$

The power spectrum of the velocity fluctuation is defined as follows:

$$C_V(\omega) = \int_{-\infty}^\infty \mathrm{d}tC_V(t)\exp(-i\omega t) \tag{C.6}$$

$$= 2\mathrm{Re}\left[\hat{C}_V(\omega)\right]. \tag{C.7}$$

Inserting the Laplace transform of the VACF (Eq. (C.3)) into Eq. (C.7) leads to

$$C_V(\omega) = \frac{2k_BT\mathrm{Re}\zeta(\omega)}{\omega^2M_{\text{eff}}^2 + 2\omega M_{\text{eff}}\mathrm{Im}\zeta(\omega) + |\zeta(\omega)|^2}. \tag{C.8}$$

The mean-square displacement (MSD) in one spatial direction is evaluated with the VACF as follows:

$$\langle \Delta x(t)^2\rangle = 2\int_0^t (t-s)C_V(s)\mathrm{d}s. \tag{C.9}$$

To numerically calculate the inverse Fourier transform in Eq. (C.5) with a high accuracy, the modified Filon algorithm [89] is used. The MSD is calculated for the obtained VACF using Eq. (C.9).

When the perturbative flow around the particle in a Newtonian solvent is neglected, the Brownian motion is described by the standard Markovian Langevin equation. By setting $M_{\text{eff}} = M$ and $\zeta(t) = \zeta_s\delta(t)$ with $\zeta_s = 6\pi\eta_s a$ in Eq. (C.1), the VACF and MSD are obtained as follows:

$$C_V(t) = \frac{k_BT}{M}\exp\left(-\frac{t}{\tau_B}\right), \tag{C.10}$$

$$\langle \Delta x(t)^2\rangle = \frac{2k_BT}{\zeta_s}\left[t + \tau_B\left(\exp\left(-\frac{t}{\tau_B}\right) - 1\right)\right], \tag{C.11}$$

where $\tau_B = M/\zeta_s$ is the correlation time in the standard Langevin equation. For short timescales $t \ll \tau_B$, $\langle \Delta x(t)^2\rangle = (k_BT/M)t^2$ due to the ballistic motion is obtained. For long timescales $t \gg \tau_B$, $\langle \Delta x(t)^2\rangle = 2Dt$, which includes the Stokes–Einstein relation $D = k_BT/\zeta$, is obtained.

For a Newtonian fluid, by substituting $\eta^*(\omega) = \eta_s$ into Eq. (C.4), the VACF in the time domain can be expressed in an integral form as follows [90,24]:

$$C_V(t) = \frac{k_B T}{M_{\text{eff}}} \int_0^\infty \frac{\mathrm{d}x}{\pi} \frac{\sigma_0 \sqrt{x} \exp\left(-x\,|t|/\tau_{B,\text{eff}}\right)}{|1-x|^2 + \sigma_0^2 x}, \tag{C.12}$$

where $\tau_{B,\text{eff}} = M_{\text{eff}}/\zeta_s$, $\sigma_0 = \left(9\rho_f/\left(2\rho_p + \rho_f\right)\right)^{1/2}$, and ρ_p is the mass density of the particle. For a neutrally buoyant particle, Eq. (C.12) is reduced to

$$C_V(t) = \frac{2k_B T}{3M} \int_0^\infty \frac{\mathrm{d}x}{3\pi} \frac{\sqrt{x} \exp\left(-x\nu\,|t|/a^2\right)}{1 + x/3 + x^2/9}. \tag{C.13}$$

The analytic solution of Eq. (C.12) is obtained when $\rho_p/\rho_f < 5/8$ [91,13,62]. For this case, the MSD in a closed form is obtained [12, 92,93]. In the long-time region at $t \gg \tau_{B,\text{eff}}$, the VACF approaches

$$C_V(t) \approx \frac{k_B T}{12\rho_f (\pi\nu)^{3/2}} t^{-3/2}, \tag{C.14}$$

which is the well-known long-time tail.

For an Oldroyd-B fluid, the complex viscosity is

$$\eta^*(\omega) = \eta_s + \frac{\eta_p}{1 + i\omega\lambda}, \tag{C.15}$$

where the second term is the contribution from the Maxwell model of Eq. (38). The VACF is obtained by numerically inverting Eq. (C.3) with $\eta^*(\omega)$ of Eq. (C.15).

Appendix D. Rotational diffusion

Analogously to the VACF, the one-directional rotational velocity autocorrelation function (RVACF) of a sphere $C_R(t) = \langle \Omega_x(t)\Omega_x(0)\rangle$ is

$$I_p \frac{\mathrm{d}C_R}{\mathrm{d}t} = -\int_0^t \mathrm{d}s \zeta_r(t-s) C_R(s), \tag{D.1}$$

where $\zeta_r(t)$ is a time-dependent rotational friction coefficient. The Laplace transform of Eq. (D.1) leads to

$$\hat{C}_R(\omega) = \frac{k_B T}{i\omega I_p + \zeta_r(\omega)}, \tag{D.2}$$

where $C_R(t=0) = \langle \Omega_x^2 \rangle = k_B T/I_p$ is used; the friction coefficient is represented as follows [85,59]:

$$\zeta_r(\omega) = 8\pi a^3 \eta^*(\omega) \left(1 + \frac{i\omega\rho_f a^2/3\eta^*(\omega)}{1 + a\sqrt{i\omega\rho_f/\eta^*(\omega)}}\right), \tag{D.3}$$

leading to [59]

$$\hat{C}_R(\omega) = \frac{k_B T \tau_f}{I_p} \frac{1 + \sqrt{i\omega\tau_f}}{3x + 3x\sqrt{i\omega\tau_f} + i\omega\tau_f(1+x) + i\omega\tau_f\sqrt{i\omega\tau_f}}, \tag{D.4}$$

where $\tau_f = a^2\rho_f/\eta^*(\omega)$ and $x = 5\rho_f/\rho_p$. Similar to the VACF, the RVACF $C_R(t)$ is obtained by the inversion of $\hat{C}_R(\omega)$ with an explicit expression of $\eta^*(\omega)$.

By setting $\zeta_r(t) = 8\pi\eta_s a^3 \delta(t)$, Eq. (D.1) can be reduced to the standard rotational Langevin equation; in this case, the RVACF is obtained as follows:

$$C_R(t) = \frac{k_B T}{I_p} \exp\left(-\frac{t}{\tau_r}\right), \tag{D.5}$$

where $\tau_r = I_p/(8\pi\eta_s a^3)$. For a Newtonian fluid with $\eta^*(\omega) = \eta_s$, the RVACF in the time domain is expressed in an integral form as follows [24]:

$$C_R(t) = \frac{k_B T}{8\pi\eta a^3} \frac{1}{\tau_s} \int_0^\infty \frac{\mathrm{d}x}{3\pi} \exp\left(-\frac{xt}{\tau_s}\right) \left[\frac{x^{3/2}}{\left[1 - \left(\frac{\tau_r}{\tau_s} + \frac{1}{3}\right)x\right]^2 + x\left(1 - \frac{\tau_r}{\tau_s}x\right)^2}\right]. \tag{D.6}$$

In the long-time region $t \gg \tau_r$, the RVACF approaches

$$C_R(t) \approx \frac{\pi k_B T}{32\rho_f(\pi\nu)^{5/2}} t^{-5/2}. \tag{D.7}$$

For an Oldroyd-B fluid, the RVACF is obtained using the complex viscosity of Eq. (C.15).

To analyze the rotational displacement of a particle, the motion of an initial orientational unit vector $\boldsymbol{p}$ fixed to the particle is considered; it evolves according to the angular velocity of the particle as follows:

$$\frac{\mathrm{d}\boldsymbol{p}}{\mathrm{d}t} = \boldsymbol{\Omega} \times \boldsymbol{p}. \tag{D.8}$$

Following [70–72], the vector rotational displacement is defined as follows:

$$\Delta\boldsymbol{\phi}(t) = \int_0^t \boldsymbol{\omega}(s)\mathrm{d}s, \tag{D.9}$$

where $\boldsymbol{\omega} = \boldsymbol{p} \times \mathrm{d}\boldsymbol{p}/\mathrm{d}t = \boldsymbol{\Omega} - (\boldsymbol{p}\cdot\boldsymbol{\Omega})\boldsymbol{p}$. Since $\boldsymbol{p}$ moves on the surface of a unit sphere, both $\boldsymbol{p}$ and $\boldsymbol{\omega}$ have two degrees of freedom, respectively, meaning that $\langle\boldsymbol{\omega}^2\rangle = \langle\boldsymbol{\Omega}^2\rangle - \langle(\boldsymbol{p}\cdot\boldsymbol{\Omega})^2\rangle = 2k_BT/I_p$. The rotational mean-square displacement (RMSD) is defined as $\langle\Delta\boldsymbol{\phi}^2(t)\rangle$. The definition of $\Delta\boldsymbol{\phi}$ of Eq. (D.9) leads to

$$\langle\Delta\boldsymbol{\phi}^2(t)\rangle = 2\int_0^t (t-s)\,\langle\boldsymbol{\omega}(t)\cdot\boldsymbol{\omega}(0)\rangle\mathrm{d}s. \tag{D.10}$$

By assuming a relation $\langle\boldsymbol{\omega}(t)\cdot\boldsymbol{\omega}(0)\rangle \approx 2C_R(t)$, the RMSD can be evaluated with the RVACF. As an example, for the Markovianized Langevin equation, substituting the RVACF of Eq. (D.5) into Eq. (D.10) yields

$$\left\langle\Delta\boldsymbol{\phi}^2(t)\right\rangle = 4D_r\left[t + \tau_r\left(\exp\left(-\frac{t}{\tau_r}\right) - 1\right)\right], \tag{D.11}$$

which has an asymptote that is approximately equal to $4D_rt$ at $t \gg \tau_r$, which includes the Stokes–Einstein–Debye relation $D_r = k_BT/(8\pi\eta_s a^3)$. For short timescales $t \ll \tau_r$, $\left\langle\Delta\boldsymbol{\phi}^2(t)\right\rangle = 2\left(k_BT/I_p\right)t^2$ is expected.

Appendix E. Fitting model for mean-square displacement

To fit the MSD data, we use a model function introduced in [43]:

$$\langle\Delta\boldsymbol{R}^2(t)\rangle = 6D\lambda f_{LE}(t/\lambda) + \int_0^\infty \frac{\mathrm{d}\tau}{\tau} h(\tau) f_{mKV}(t/\tau), \tag{E.1}$$

$$f_{\mathrm{LE}}(t/\lambda) = \frac{t}{\lambda} + \left(e^{-t/\lambda} - 1\right), \tag{E.2}$$

$$f_{\mathrm{mKV}}(t/\tau) = 1 - \left(1 + \frac{t}{\tau}\right)e^{-t/\tau}, \tag{E.3}$$

$$h(\tau) = \sum_{j=1}^{n} g_j \tau^{\alpha_j} H(\tau_j - \tau)H(\tau - \tau_{j-1}). \tag{E.4}$$

Here, $f_{\mathrm{LE}}(t/\lambda)$ is the MSD function derived from the Markovian Langevin equation, which shows a ballistic behavior for $(t/\lambda)^2/2$ at $t \ll \lambda$ and normal diffusive behavior at $t \gg \lambda$; $f_{\mathrm{mKV}}(t/\tau)$ is the modified Kelvin-Voigt compliance, which shows a ballistic behavior for $f_{\mathrm{mKV}} \propto (t/\tau)^2/2$ at $t \ll \tau$ and a plateau of $f_{mKV} \to 1$ at $t \gg \tau$; and $h(\tau)$ is a piece-wise power-law spectrum [94] with $\tau_j > \tau_{j-1}$, where $H(.)$ is the Heaviside step function. By assuming that $h(\tau)$ is continuous, it can be found that a relation $h(\tau_j) = g_j\tau_j^{\alpha_j} = g_{j+1}\tau_j^{\alpha_{j+1}}$ holds; from this relation, weights g_j for $1 < j \le n$ are determined from the other parameters as follows:

$$g_j = g_1 \prod_{k=1}^{j-1} \tau_k^{\alpha_k - \alpha_{k+1}}. \tag{E.5}$$

Integrating the second term in Eq. (E.1) leads to

$$\int_0^\infty \frac{\mathrm{d}\tau}{\tau} h(\tau) f_{mKV}(t/\tau) = \sum_{j=1}^{n} g_j \int_{\tau_{j-1}}^{\tau_j} \mathrm{d}\tau\,\tau^{\alpha_j - 1}\left[1 - \left(1 + \frac{t}{\tau}\right)e^{-t/\tau}\right] \tag{E.6}$$

$$= \sum_{j=1}^{n} g_j \left[\frac{\tau_j^{\alpha_j} - \tau_{j-1}^{\alpha_j}}{\alpha_j} - t^{\alpha_j} \left(\Gamma\left(-\alpha_j, \frac{t}{\tau_j}\right) - \Gamma\left(-\alpha_j, \frac{t}{\tau_{j-1}}\right) + \Gamma\left(1-\alpha_j, \frac{t}{\tau_j}\right) - \Gamma\left(1-\alpha_j, \frac{t}{\tau_{j-1}}\right) \right) \right], \tag{E.7}$$

where $\Gamma(a,x)$ is the upper incomplete gamma function. By assuming that $\lambda = \tau_n$ (the longest relaxation time in $H(\tau)$), we have $2n+3$ free parameters: $\{D, g_1, \alpha_1, \ldots, \alpha_n, \tau_0, \ldots, \tau_n\}$. Eqs. (E.2) and (E.3) are analytically Laplace transformed. The Laplace transform of Eq. (E.1) is

$$\widehat{\langle \Delta \boldsymbol{R}^2 \rangle}(s = i\omega) = \frac{6D}{(i\omega)^2 (i\omega\lambda + 1)} + \sum_{j=1}^{n} g_j \int_{\tau_{j-1}}^{\tau_j} \mathrm{d}\tau \frac{\tau^{\alpha_j - 1}}{(i\omega)(i\omega\tau + 1)^2}. \tag{E.8}$$

The integration of the last term of Eq. (E.8) is expressed with the hypergeometric function as follows:

$$\int_{\tau_{j-1}}^{\tau_j} \mathrm{d}\tau \frac{\tau^{\alpha_j - 1}}{(i\omega\tau + 1)^2} = \frac{\tau_j^{\alpha_j} {}_2F_1(2, \alpha_j, \alpha_j + 1; -(i\omega)\tau_j) - \tau_j^{\alpha_{j-1}} {}_2F_1(2, \alpha_j, \alpha_j + 1; -(i\omega)\tau_{j-1})}{\alpha_j}. \tag{E.9}$$

References

[1] W.B. Russel, W. Russel, D.A. Saville, W.R. Schowalter, Colloidal Dispersions, Cambridge University Press, 1991.
[2] J. Mewis, N.J. Wagner, Colloidal Suspension Rheology, Cambridge University Press, 2012.
[3] T.G. Mason, D.A. Weitz, Optical measurements of frequency-dependent linear viscoelastic moduli of complex fluids, Phys. Rev. Lett. 74 (7) (1995) 1250–1253, https://doi.org/10.1103/PhysRevLett.74.1250, https://link.aps.org/doi/10.1103/PhysRevLett.74.1250.
[4] T.G. Mason, K. Ganesan, J.H. van Zanten, D. Wirtz, S.C. Kuo, Particle tracking microrheology of complex fluids, Phys. Rev. Lett. 79 (17) (1997) 3282–3285, https://doi.org/10.1103/PhysRevLett.79.3282, https://link.aps.org/doi/10.1103/PhysRevLett.79.3282.
[5] M.J. Solomon, Q. Lu, Rheology and dynamics of particles in viscoelastic media, Curr. Opin. Colloid Interface Sci. 6 (5–6) (2001) 430–437, https://doi.org/10.1016/S1359-0294(01)00111-X, https://linkinghub.elsevier.com/retrieve/pii/S135902940100111X.
[6] J.R. Gomez-Solano, C. Bechinger, Probing linear and nonlinear microrheology of viscoelastic fluids, Europhys. Lett. 108 (5) (2014) 54008, https://doi.org/10.1209/0295-5075/108/54008, arXiv:1412.4897, http://stacks.iop.org/0295-5075/108/i=5/a=54008?key=crossref.27f4f25da9076ea092bf9eeaaeb41970.
[7] Y. Kimura, Microrheology of soft matter, J. Phys. Soc. Jpn. 78 (4) (2009) 041005.
[8] T.M. Squires, T.G. Mason, Fluid mechanics of microrheology, Annu. Rev. Fluid Mech. 42 (2010) 413–438.
[9] T.A. Waigh, Advances in the microrheology of complex fluids, Rep. Prog. Phys. 79 (7) (2016) 074601.
[10] B. Felderhof, Estimating the viscoelastic moduli of a complex fluid from observation of Brownian motion, J. Chem. Phys. 131 (16) (2009) 164904.
[11] T. Indei, J.D. Schieber, A. Córdoba, E. Pilyugina, Treating inertia in passive microbead rheology, Phys. Rev. E 85 (2) (2012) 021504.
[12] V. Vladimirsky, Y. Terletzky, Hydrodynamical theory of translational Brownian motion, Zh. Èksp. Teor. Fiz. 15 (1945) 258–263.
[13] E.J. Hinch, Application of the Langevin equation to fluid suspensions, J. Fluid Mech. 72 (3) (1975) 499–511.
[14] A.J. Ladd, Short-time motion of colloidal particles: numerical simulation via a fluctuating lattice-Boltzmann equation, Phys. Rev. Lett. 70 (9) (1993) 1339.
[15] A.J. Ladd, Numerical simulations of particulate suspensions via a discretized Boltzmann equation. Part 2. Numerical results, J. Fluid Mech. 271 (1994) 311–339.
[16] P.J. Atzberger, P.R. Kramer, C.S. Peskin, A stochastic immersed boundary method for fluid-structure dynamics at microscopic length scales, J. Comput. Phys. 224 (2) (2007) 1255–1292.
[17] P.J. Atzberger, Stochastic Eulerian Lagrangian methods for fluid–structure interactions with thermal fluctuations, J. Comput. Phys. 230 (8) (2011) 2821–2837.
[18] S. Delong, F.B. Usabiaga, R. Delgado-Buscalioni, B.E. Griffith, A. Donev, Brownian dynamics without Green's functions, J. Chem. Phys. 140 (13) (2014) 134110.
[19] F.B. Usabiaga, I. Pagonabarraga, R. Delgado-Buscalioni, Inertial coupling for point particle fluctuating hydrodynamics, J. Comput. Phys. 235 (2013) 701–722.
[20] F.B. Usabiaga, R. Delgado-Buscalioni, B.E. Griffith, A. Donev, Inertial coupling method for particles in an incompressible fluctuating fluid, Comput. Methods Appl. Mech. Eng. 269 (2014) 139–172.
[21] B. Delmotte, E.E. Keaveny, Simulating Brownian suspensions with fluctuating hydrodynamics, J. Chem. Phys. 143 (24) (2015) 244109.
[22] P. Ahlrichs, B. Dünweg, Lattice-Boltzmann simulation of polymer-solvent systems, Int. J. Mod. Phys. C 9 (08) (1998) 1429–1438.
[23] P. Ahlrichs, B. Dünweg, Simulation of a single polymer chain in solution by combining lattice Boltzmann and molecular dynamics, J. Chem. Phys. 111 (17) (1999) 8225–8239.
[24] T. Iwashita, Y. Nakayama, R. Yamamoto, A numerical model for Brownian particles fluctuating in incompressible fluids, J. Phys. Soc. Jpn. 77 (7) (2008) 1–6, https://doi.org/10.1143/JPSJ.77.074007, arXiv:0804.0627.
[25] T. Iwashita, Y. Nakayama, R. Yamamoto, Velocity autocorrelation function of fluctuating particles in incompressible fluids: toward direct numerical simulation of particle dispersions, Prog. Theor. Phys. Suppl. 178 (178) (2009) 86–91, https://doi.org/10.1143/ptps.178.86, arXiv:0810.4360, http://arxiv.org/abs/0810.4360.
[26] T. Iwashita, R. Yamamoto, Direct numerical simulations for non-Newtonian rheology of concentrated particle dispersions, Phys. Rev. E 80 (6) (2009) 061402, https://doi.org/10.1103/PhysRevE.80.061402, arXiv:0905.0130, https://link.aps.org/doi/10.1103/PhysRevE.80.061402.
[27] T. Iwashita, T. Kumagai, R. Yamamoto, A direct numerical simulation method for complex modulus of particle dispersions, Eur. Phys. J. E 32 (4) (2010) 357–363, https://doi.org/10.1140/epje/i2010-10638-7, http://link.springer.com/10.1140/epje/i2010-10638-7.
[28] Y. Matsuoka, T. Fukasawa, K. Higashitani, R. Yamamoto, Effect of hydrodynamic interactions on rapid Brownian coagulation of colloidal dispersions, Phys. Rev. E 86 (5) (2012) 051403, https://doi.org/10.1103/PhysRevE.86.051403, https://link.aps.org/doi/10.1103/PhysRevE.86.051403.
[29] N.K. Voulgarakis, S. Satish, J.W. Chu, Modeling the nanoscale viscoelasticity of fluids by bridging non-Markovian fluctuating hydrodynamics and molecular dynamics simulations, J. Chem. Phys. 131 (23) (2009) 234115, https://doi.org/10.1063/1.3273210, http://aip.scitation.org/doi/10.1063/1.3273210.
[30] N.K. Voulgarakis, S. Satish, J.W. Chu, Modelling the viscoelasticity and thermal fluctuations of fluids at the nanoscale, Mol. Simul. 36 (7–8) (2010) 552–559, https://doi.org/10.1080/08927022.2010.486832.
[31] C. Hohenegger, S.A. McKinley, Fluid-particle dynamics for passive tracers advected by a thermally fluctuating viscoelastic medium, J. Comput. Phys. 340 (2017) 688–711, https://doi.org/10.1016/j.jcp.2017.03.053.
[32] A. Vázquez-Quesada, M. Ellero, P. Español, Smoothed particle hydrodynamic model for viscoelastic fluids with thermal fluctuations, Phys. Rev. E, Stat. Nonlinear Soft Matter Phys. 79 (5) (2009) 056707, https://doi.org/10.1103/PhysRevE.79.056707.
[33] H.C. Öttinger, Beyond Equilibrium Thermodynamics, John Wiley & Sons, 2005.
[34] A. Vázquez-Quesada, M. Ellero, P. Español, A SPH-based particle model for computational microrheology, Microfluid. Nanofluid. 13 (2) (2012) 249–260, https://doi.org/10.1007/s10404-012-0954-2, http://link.springer.com/10.1007/s10404-012-0954-2.

[35] M. Hütter, M.A. Hulsen, P.D. Anderson, Fluctuating viscoelasticity, J. Non-Newton. Fluid Mech. 256 (February 2018) 42–56, https://doi.org/10.1016/j.jnnfm.2018.02.012.
[36] M. Hütter, H.C. Öttinger, Gauge conditions on the "square root" of the conformation tensor in rheological models, J. Non-Newton. Fluid Mech. 271 (May 2019) 104145, https://doi.org/10.1016/j.jnnfm.2019.104145.
[37] M. Hütter, M.A. Carrozza, M.A. Hulsen, P.D. Anderson, Behavior of viscoelastic models with thermal fluctuations, Eur. Phys. J. E 43 (5) (2020) 24, https://doi.org/10.1140/epje/i2020-11948-9, http://link.springer.com/10.1140/epje/i2020-11948-9.
[38] M. Hütter, P.D. Olmsted, D.J. Read, Fluctuating viscoelasticity based on a finite number of dumbbells, Eur. Phys. J. E 43 (11) (2020) 1–14.
[39] Y. Nakayama, R. Yamamoto, Simulation method to resolve hydrodynamic interactions in colloidal dispersions, Phys. Rev. E 71 (3) (2005) 036707, https://doi.org/10.1103/PhysRevE.71.036707.
[40] K. Kim, Y. Nakayama, R. Yamamoto, A smoothed profile method for simulating charged colloidal dispersions, Comput. Phys. Commun. 169 (1–3) (2005) 104–106.
[41] Y. Nakayama, K. Kim, R. Yamamoto, Simulating (electro)hydrodynamic effects in colloidal dispersions: smoothed profile method, Eur. Phys. J. E 26 (4) (2008) 361–368, https://doi.org/10.1140/epje/i2007-10332-y, arXiv:cond-mat/0601322, http://link.springer.com/10.1140/epje/i2007-10332-y.
[42] R. Yamamoto, Y. Nakayama, K. Kim, Smoothed profile method to simulate colloidal particles in complex fluids, Int. J. Mod. Phys. C 20 (09) (2009) 1457–1465.
[43] M. Karim, S.C. Kohale, T. Indei, J.D. Schieber, R. Khare, Determination of viscoelastic properties by analysis of probe-particle motion in molecular simulations, Phys. Rev. E 86 (5) (2012) 051501.
[44] J.G. Ethier, P. Nourian, R. Islam, R. Khare, J.D. Schieber, Microrheology analysis in molecular dynamics simulations: finite box size correction, J. Rheol. 65 (6) (2021) 1255–1267.
[45] L.D. Landau, E.M. Lifshitz, Statistical Physics, Part 1, Elsevier, 1980.
[46] A. Vázquez-Quesada, M. Ellero, P. Español, Consistent scaling of thermal fluctuations in smoothed dissipative particle dynamics, J. Chem. Phys. 130 (3) (2009), https://doi.org/10.1063/1.3050100.
[47] S. Paul, B. Roy, A. Banerjee, Free and confined Brownian motion in viscoelastic Stokes-Oldroyd B fluids, J. Phys. Condens. Matter 30 (34) (2018) 345101, https://doi.org/10.1088/1361-648X/aad421, http://stacks.iop.org/0953-8984/30/i=34/a=345101?key=crossref.d073d2bbf1fa0dd65a7ce25be7069623.
[48] S. Paul, A. Kundu, A. Banerjee, Active microrheology to determine viscoelastic parameters of Stokes-Oldroyd B fluids using optical tweezers, J. Phys. Commun. 3 (3) (2019) 035002, https://doi.org/10.1088/2399-6528/ab0833, arXiv:1811.01262, http://stacks.iop.org/2399-6528/3/i=3/a=035002?key=crossref.7a387c8953ecab8ed700c54a711de9e3.
[49] M.A. Carrozza, M.A. Hulsen, M. Hütter, P.D. Anderson, Viscoelastic fluid flow simulation using the contravariant deformation formulation, J. Non-Newton. Fluid Mech. 270 (2019) 23–35.
[50] J.J. Molina, K. Otomura, H. Shiba, H. Kobayashi, M. Sano, R. Yamamoto, Rheological evaluation of colloidal dispersions using the smoothed profile method: formulation and applications, J. Fluid Mech. 792 (2016) 590–619, https://doi.org/10.1017/jfm.2016.78, http://www.journals.cambridge.org/abstract_S0022112016000781.
[51] R. Yamamoto, J.J. Molina, Y. Nakayama, Smoothed profile method for direct numerical simulations of hydrodynamically interacting particles, Soft Matter 17 (16) (2021) 4226–4253.
[52] C. Canuto, M. Hussaini, A. Quarteroni, T.A. Zang, Spectral Methods in Fluid Dynamics, Springer-Verlag, 1988.
[53] S. Delong, B.E. Griffith, E. Vanden-Eijnden, A. Donev, Temporal integrators for fluctuating hydrodynamics, Phys. Rev. E 87 (3) (2013) 033302.
[54] A.K. Sankaran, D.A. Dros, H.J. Meerman, S.J. Picken, M.T. Kreutzer, Increasing the stability of high contraction ratio flow of Boger fluids by pre-deformation, J. Non-Newton. Fluid Mech. 196 (2013) 27–35.
[55] J. Padding, A. Louis, Hydrodynamic interactions and Brownian forces in colloidal suspensions: coarse-graining over time and length scales, Phys. Rev. E 74 (3) (2006) 031402.
[56] M. Saito, M. Matsumoto, A PRNG specialized in double precision floating point numbers using an affine transition, in: Monte Carlo and Quasi-Monte Carlo Methods, 2008–2009, pp. 589–602.
[57] N.K. Ailawadi, A. Rahman, R. Zwanzig, Generalized hydrodynamics and analysis of current correlation functions, Phys. Rev. A 4 (4) (1971) 1616.
[58] J.-P. Hansen, I.R. McDonald, Theory of Simple Liquids, 3rd edition, Elsevier, Amsterdam, 2006.
[59] V. Lisy, J. Tothova, On the (hydrodynamic) memory in the theory of Brownian motion, arXiv preprint, arXiv:cond-mat/0410222, 2004.
[60] T. Li, M.G. Raizen, Brownian motion at short time scales, Ann. Phys. 525 (4) (2013) 281–295, https://doi.org/10.1002/andp.201200232, arXiv:1211.1458, http://doi.wiley.com/10.1002/andp.201200232.
[61] X. Bian, C. Kim, G.E. Karniadakis, 111 years of Brownian motion, Soft Matter 12 (30) (2016) 6331–6346, https://doi.org/10.1039/C6SM01153E, http://xlink.rsc.org/?DOI=C6SM01153E.
[62] H.J.H. Clercx, P.P.J.M. Schram, Brownian particles in shear flow and harmonic potentials: a study of long-time tails, Phys. Rev. A 46 (4) (1992) 1942–1950.
[63] P.J. Atzberger, Velocity correlations of a thermally fluctuating Brownian particle: a novel model of the hydrodynamic coupling, Phys. Lett. A 351 (4–5) (2006) 225–230.
[64] H. Hasimoto, On the periodic fundamental solutions of the Stokes equations and their application to viscous flow past a cubic array of spheres, J. Fluid Mech. 5 (02) (1959) 317, https://doi.org/10.1017/S0022112059000222.
[65] A.S. Sangani, A. Acrivos, Slow flow through a periodic array of spheres, Int. J. Multiph. Flow 8 (4) (1982) 343–360.
[66] B. Dünweg, K. Kremer, Molecular dynamics simulation of a polymer chain in solution, J. Chem. Phys. 99 (9) (1993) 6983–6997.
[67] I.C. Yeh, G. Hummer, System-size dependence of diffusion coefficients and viscosities from molecular dynamics simulations with periodic boundary conditions, J. Phys. Chem. B 108 (40) (2004) 15873–15879, https://doi.org/10.1021/jp0477147.
[68] D. Heyes, System size dependence of the transport coefficients and Stokes–Einstein relationship of hard sphere and Weeks–Chandler–Andersen fluids, J. Phys. Condens. Matter 19 (37) (2007) 376106.
[69] A.A. Zick, G.M. Homsy, Stokes flow through periodic arrays of spheres, J. Fluid Mech. 115 (1) (1982) 13–26, https://doi.org/10.1017/S0022112082000627.
[70] S. Kämmerer, W. Kob, R. Schilling, Dynamics of the rotational degrees of freedom in a supercooled liquid of diatomic molecules, Phys. Rev. E 56 (5) (1997) 5450.
[71] M.G. Mazza, N. Giovambattista, H.E. Stanley, F.W. Starr, Connection of translational and rotational dynamical heterogeneities with the breakdown of the Stokes-Einstein and Stokes-Einstein-Debye relations in water, Phys. Rev. E 76 (3) (2007) 031203, https://doi.org/10.1103/PhysRevE.76.031203.
[72] G.L. Hunter, K.V. Edmond, M.T. Elsesser, E.R. Weeks, Tracking rotational diffusion of colloidal clusters, Opt. Express 19 (18) (2011) 17189, https://doi.org/10.1364/oe.19.017189, arXiv:1107.2614.
[73] M. Grimm, S. Jeney, T. Franosch, Brownian motion in a Maxwell fluid, Soft Matter 7 (5) (2011) 2076–2084, https://doi.org/10.1039/c0sm00636j, http://xlink.rsc.org/?DOI=c0sm00636j.
[74] Y.L. Raikher, V.V. Rusakov, Theory of Brownian motion in a Jeffreys fluid, J. Exp. Theor. Phys. 111 (5) (2010) 883–889, https://doi.org/10.1134/S1063776110110191, http://link.springer.com/10.1134/S1063776110110191.
[75] Y.L. Raikher, V.V. Rusakov, R. Perzynski, Brownian motion in a viscoelastic medium modelled by a Jeffreys fluid, Soft Matter 9 (45) (2013) 10857–10865, https://doi.org/10.1039/c3sm51956b, http://xlink.rsc.org/?DOI=c3sm51956b.
[76] V.V. Rusakov, Y.L. Raikher, R. Perzynski, Brownian motion in the fluids with complex rheology, Math. Model. Nat. Phenom. 10 (4) (2015) 1–43, https://doi.org/10.1051/mmnp/201510401, http://www.mmnp-journal.org/10.1051/mmnp/201510401.

[77] J.H. Van Zanten, K.P. Rufener, Brownian motion in a single relaxation time Maxwell fluid, Phys. Rev. E 62 (4B) (2000) 5389–5396, https://doi.org/10.1103/PhysRevE.62.5389.
[78] S.C. Weber, A.J. Spakowitz, J.A. Theriot, Bacterial chromosomal loci move subdiffusively through a viscoelastic cytoplasm, Phys. Rev. Lett. 104 (23) (2010) 238102, https://doi.org/10.1103/PhysRevLett.104.238102, https://link.aps.org/doi/10.1103/PhysRevLett.104.238102.
[79] E.R. Weeks, D.A. Weitz, Subdiffusion and the cage effect studied near the colloidal glass transition, Chem. Phys. 284 (1–2) (2002) 361–367, https://doi.org/10.1016/S0301-0104(02)00667-5, arXiv:cond-mat/0111073v1, https://linkinghub.elsevier.com/retrieve/pii/S0301010402006675.
[80] K. Xu, M.G. Forest, I. Klapper, On the correspondence between creeping flows of viscous and viscoelastic fluids, J. Non-Newton. Fluid Mech. 145 (2–3) (2007) 150–172.
[81] J.D. Schieber, A. Córdoba, T. Indei, The analytic solution of Stokes for time-dependent creeping flow around a sphere: application to linear viscoelasticity as an ingredient for the generalized Stokes–Einstein relation and microrheology analysis, J. Non-Newton. Fluid Mech. 200 (2013) 3–8.
[82] T. Indei, J.D. Schieber, A. Córdoba, Competing effects of particle and medium inertia on particle diffusion in viscoelastic materials, and their ramifications for passive microrheology, Phys. Rev. E 85 (4) (2012) 041504.
[83] Y. Matsuoka, Y. Nakayama, T. Kajiwara, Effects of viscoelasticity on shear-thickening in dilute suspensions in a viscoelastic fluid, Soft Matter 16 (3) (2020) 728–737.
[84] Y. Matsuoka, Y. Nakayama, T. Kajiwara, Prediction of shear thickening of particle suspensions in viscoelastic fluids by direct numerical simulation, J. Fluid Mech. 913 (2021).
[85] L.D. Landau, E.M. Lifshitz, Fluid Mechanics, Pergamon Press, London, 1959.
[86] A. Vázquez-Quesada, M. Ellero, Sph modeling and simulation of spherical particles interacting in a viscoelastic matrix, Phys. Fluids 29 (12) (2017) 121609.
[87] A. Vázquez-Quesada, P. Español, R.I. Tanner, M. Ellero, Shear thickening of a non-colloidal suspension with a viscoelastic matrix, J. Fluid Mech. 880 (2019) 1070–1094, https://doi.org/10.1017/jfm.2019.753, https://www.cambridge.org/core/product/identifier/S0022112019007535/type/journal_article.
[88] C.W. Gardiner, Stochastic Methods: A Handbook for the Natural and Social Sciences, Springer, 2009.
[89] T. Blochowicz, Broadband Dielectric Spectroscopy in Neat and Binary Molecular Glass Formers: Frequency and Time Domain Spectroscopy, Non-resonant Spectral Hole Burning, Logos-Verlag, 2003.
[90] K. Ohbayashi, T. Kohno, H. Utiyama, Photon correlation spectroscopy of the non-Markovian Brownian motion of spherical particles, Phys. Rev. A 27 (5) (1983) 2632.
[91] A. Widom, Velocity fluctuations of a hard-core Brownian particle, Phys. Rev. A 3 (4) (1971) 1394.
[92] G. Paul, P. Pusey, Observation of a long-time tail in Brownian motion, J. Phys. A, Math. Gen. 14 (12) (1981) 3301.
[93] B. Lukić, S. Jeney, C. Tischer, A.J. Kulik, L. Forró, E.L. Florin, Direct observation of nondiffusive motion of a Brownian particle, Phys. Rev. Lett. 95 (16) (2005) 160601, https://doi.org/10.1103/PhysRevLett.95.160601.
[94] M. Baumgaertel, A. Schausberger, H. Winter, The relaxation of polymers with linear flexible chains of uniform length, Rheol. Acta 29 (5) (1990) 400–408.